

# Modulating interfacial charge distribution of $\text{Ni}_2\text{P}-\text{NiSe}_2$ by multiple interface engineering for accelerating water splitting with industry-level activity and stability

Jin-Tao Ren, Lei Chen, Hao-Yu Wang, Wen-Wen Tian, Si-Xiang Zhai, Yi Feng, Zhong-Yong Yuan\*

School of Materials Science and Engineering, Smart Sensing Interdisciplinary Science Center, Key Laboratory of Advanced Energy Materials Chemistry (Ministry of Education), Nankai University, Tianjin 300350, China



## ARTICLE INFO

**Keywords:**  
Interface engineering  
Electronic redistribution  
Heterostructures  
Hydrogen evolution  
Electrocatalysis

## ABSTRACT

Suitable electrocatalysts for industrial water splitting can veritably promote practical hydrogen applications. Guided by density functional theory calculations, the interface-rich  $\text{Ni}_2\text{P}-\text{NiSe}_2$  nanoparticles anchored on amorphous  $\text{MoO}_x$  nanorods on nickel foam ( $\text{Ni}_2\text{P}-\text{NiSe}_2/\text{MoO}_x/\text{NF}$ ) are fabricated.  $\text{Ni}_2\text{P}-\text{NiSe}_2/\text{MoO}_x/\text{NF}$  exhibits exceptional HER performance with overpotentials of 23 and 263 mV at 10 and 500 mA  $\text{cm}^{-2}$ , outperforming most reported non-Pt based electrocatalysts reported hitherto. Remarkably, the excellent oxygen evolution activity (241 mV at 10 mA  $\text{cm}^{-2}$ ) of  $\text{Ni}_2\text{P}-\text{NiSe}_2/\text{MoO}_x/\text{NF}$  further realizes the full electrolyzer requiring the voltage of 1.63 V at 50 mA  $\text{cm}^{-2}$  with robust stability (1000 h at 20 mA  $\text{cm}^{-2}$ ) in 1.0 M KOH. At industrial conditions (30% KOH, 65 °C), only 2.02 V is required to reach 1000 mA  $\text{cm}^{-2}$  with satisfying durability (200 h at 200 mA  $\text{cm}^{-2}$ ). When deployed in anion exchange membrane water electrolyzer, the catalyst achieves 1.3 A  $\text{cm}^{-2}$  at 2.7 V, associated with the prolonged stability.

## 1. Introduction

Hydrogen ( $\text{H}_2$ ) generated from electrocatalytic water splitting is considered as an attractive alternative energy source to replace conventional fossil fuels because it's clean, efficient and renewable nature [1,2]. Presently, electrocatalysts based on platinum group metals (PGMs) are still the benchmark catalysts for hydrogen evolution reaction (HER), whilst their widespread application is constrained by their limited availability and high cost. Furthermore, even PGMs catalysts, due to the inherent sluggishness of the  $\text{H}_2\text{O}$  dissociation step (Volmer reaction:  $\text{H}_2\text{O} + \text{e}^- + * \rightarrow \text{H}^* + \text{OH}^-$ ), always exhibit 2-3 orders of lower activity in alkaline media compared to acidic electrolytes [3,4]. Consequently, the quest for highly efficient electrocatalysts derived from abundant elements to drive alkaline HER has becoming an urgent imperative. To date, various transition metal-based electrocatalysts, encompassing oxides, hydroxides, phosphides, sulfides, carbides, nitrides, and their alloys, have been extensively synthesized and have demonstrated promising HER activities. However, for most of these catalysts, their performance remains unsatisfactory, and a substantial

activity gap persists in comparison to the commercial benchmark of Pt/C. This performance deficit arises from their inherently low intrinsic activity and a paucity of active sites required to facilitate the multiple reaction steps involved in alkaline HER [5,6]. Hence, there is an immediate need for the development of efficient synthetic methodologies to engineer PGM-free catalysts that can rival Pt in performance for alkaline hydrogen production.

Significant research endeavors have been dedicated to the development of efficient substitutions, among them, first-row 3d transition metal-based phosphides as cost-effective HER electrocatalysts have garnered substantial attention due to their remarkable intrinsic activity, excellent conductivity, and tunable structure/composition [7,8]. Recently, engineering heterogeneous phosphide structures or constructing heterostructures with electronegative P atoms to capture intermediate  $\text{H}^*$  has emerging as a pivotal strategy to enhance the HER activity of metal phosphides, which should be primarily ascribed to the synergistic effect stemming from the interaction between distinct components and the tailored electronic band structures [9,10]. However, despite these advancements, the electrocatalytic performance of most

\* Corresponding author.

E-mail address: [zyuan@nankai.edu.cn](mailto:zyuan@nankai.edu.cn) (Z.-Y. Yuan).

heterostructure-based metal phosphides toward alkaline HER is still inferior to PGM catalysts because of poor  $\text{H}_2\text{O}$  adsorption capability and the substantial energy barrier for  $\text{H}_2\text{O}$  dissociation at the heterostructures, which are primarily determined by the electronic structure and localized charge distribution at the interface region [11]. Hence, it remains imperative to further refine the localized charge density and optimize the electronic band structure at the heterointerface of phosphide-based catalysts to enable the development of highly efficient electrocatalysts for alkaline HER [12]. However, it is still quite challenging.

Recently, noteworthy breakthroughs and substantial progress have been achieved in cost-effective transition metal-based catalysts for water splitting with promising performance under laboratory conditions, such as Pt@S–NiFe LDHs [13], Co/CoMoN/NF [14],  $\text{NiCo}_2\text{S}_4/\text{ReS}_2$  2D–2D nanosheets [15], and Fe–Co<sub>0.85</sub>Se/FeCo LDH [16]. In the pursuit of enhanced electrolysis efficiency, industrial-scale electrolyzers typically operate in 20–40 wt% KOH electrolyte and elevated temperatures ranging from 40 to 80 °C. These conditions necessitate the use of more robust and active electrode materials capable of withstanding the rigors of harsh environments. Specifically, the industrial-grade electrodes must provide enough efficient catalytic sites, rapid charge and mass transfer rates, and strong adhesion to withstand the vigorous evolution of gas bubbles [17]. However, the majority of laboratory-developed electrocatalysts are not suitable for industrial applications, primarily due to challenges related to sluggish mass transfer and inadequate adhesion between active species and conductive substrates, especially when operating at relatively high current densities exceeding 400 mA cm<sup>-2</sup> in water splitting [18,19]. To meet the stringent demands of industrial operating conditions, several key attributes are required for industrial electrocatalysts, including self-supported electrode structure, abundance of accessible active sites, favorable surface morphology to rapid gas evolution, excellent chemical and structural stability, and cost-effective and efficient synthesis process using readily available source materials [20,21]. Hence, a straightforward fabrication strategy for integrating active heterogeneous structure on the current collector as self-supported electrodes that maximize the advantages of both structure and composition is critical for enabling rapid electrochemical hydrogen production at larger current densities, particularly in industrial settings.

In this study, we employed density functional theory (DFT) predictions to establish that the localized charge density and electronic band structure at the heterointerface of  $\text{Ni}_2\text{P}-\text{NiSe}_2$  undergo significant optimization upon coupling with  $\text{MoO}_2$  substrate, thereby improving  $\text{H}_2\text{O}$  adsorption and reducing energy barrier for  $\text{H}_2\text{O}$  dissociation, and facilitating adsorption/desorption of  $\text{H}^*$ , which collectively expedite the reaction kinetics toward alkaline HER. Guided by these theoretical insights, we devised a straightforward and scalable strategy to engineer interface-rich  $\text{Ni}_2\text{P}-\text{NiSe}_2$  heterostructures, securely anchored onto amorphous  $\text{MoO}_x$  nanorods on nickel foam ( $\text{Ni}_2\text{P}-\text{NiSe}_2/\text{MoO}_x/\text{NF}$ ) as a self-supported electrode. Benefiting from the synergistic coupling interactions and the augmented intrinsic activity, the resulting  $\text{Ni}_2\text{P}-\text{NiSe}_2/\text{MoO}_x/\text{NF}$  catalyst demonstrates remarkable alkaline HER performance, surpassing the majority of known transition-metal-based HER catalysts, including the commercial benchmark of 20% Pt/C, under high current densities. Notably, the  $\text{Ni}_2\text{P}-\text{NiSe}_2/\text{MoO}_x/\text{NF}$  catalyst achieves current densities of 500 and 1000 mA cm<sup>-2</sup> at ultralow overpotentials of 263 and 424 mV, respectively, while exhibiting superior stability, even sustaining 200 h of operation in 1.0 M KOH. Due to its multiple active sites and self-supported architecture, this catalyst also exhibits excellent oxygen evolution reaction (OER) activity and stability. As a result,  $\text{Ni}_2\text{P}-\text{NiSe}_2/\text{MoO}_x/\text{NF}$  catalyst holds great promise for water-alkali electrolysis, particularly when integrated with photovoltaic cells to enable solar energy-driven water electrolysis, achieving a high gas evolution rate of 26.17  $\mu\text{L s}^{-1}$  under ambient conditions. Furthermore, it demonstrates stable performance at high current densities under industrial conditions (30% KOH, 65 °C). Lastly, when deployed in an anion exchange

membrane (AEM) water electrolyzer, the catalyst achieves a larger current density of 1.3 A cm<sup>-2</sup> at a cell voltage of 2.7 V, associated with the prolonged stability.

## 2. Experimental section

### 2.1. Synthesis of Ni-Mo-O/NF

The Ni-Mo-O-precursor nanorod arrays were grown on commercial nickel foam (NF) by a simple hydrothermal method. Prior to the growth of nanorods, NF was cleaned by acetone, ethanol and hydrochloric acid solution.  $\text{Ni}(\text{NO}_3)_2 \cdot 6 \text{H}_2\text{O}$  (2 mmol) and  $\text{Na}_2\text{MoO}_4 \cdot 2 \text{H}_2\text{O}$  (2 mmol) were dissolved in 35 mL of  $\text{H}_2\text{O}$ , and then transferred into a 50 mL Teflon-lined stainless steel autoclave. A piece of cleaned NF ( $2 \times 3 \text{ cm}^2$ ) was immersed into the solution and placed against the wall of autoclave. Subsequently, the autoclave was maintained at 150 °C for 6 h. The NF was taken out and cleaned by sonication several times to obtain Ni-Mo-O/NF precursor. The mass loading of Ni-Mo-O-precursor nanorods on NF was about 6 mg cm<sup>-2</sup> determined by weighing the mass of NF before and after the hydrothermal reaction.

### 2.2. Synthesis of $\text{Ni}_2\text{P}-\text{NiSe}_2/\text{MoO}_x/\text{NF}$

To prepare the multiple-interfaces, the obtained Ni-Mo-O/NF precursor was first treated at 400 °C for 2 h with a heating rate of 3 °C min under  $\text{H}_2/\text{Ar}$  atmosphere. Then, the obtained sample, 500 mg  $\text{NaH}_2\text{PO}_2$ , and 50 mg Se powder was put at three separate positions in one closed porcelain boat. Then, a porcelain boat was put into the furnace, ensuring that the Se powder and  $\text{NaH}_2\text{PO}_2$  were situated in the upstream. The reaction was conducted at 350 °C for 2 h, with a heating rate of 5 °C min<sup>-1</sup> under a 100 sccm flowing of Ar gas. The loading of the catalysts is about 3.5 mg cm<sup>-2</sup>.

### 2.3. Synthesis of $\text{Ni}_2\text{P}/\text{MoO}_x/\text{NF}$ and $\text{NiSe}_2/\text{MoO}_x/\text{NF}$

Similar to the preparation of  $\text{Ni}_2\text{P}-\text{NiSe}_2/\text{MoO}_x/\text{NF}$ ,  $\text{Ni}_2\text{P}/\text{MoO}_x/\text{NF}$  and  $\text{NiSe}_2/\text{MoO}_x/\text{NF}$  were also prepared simultaneously for comparison. With  $\text{NaH}_2\text{PO}_2$  as phosphorus source and Se powder as selenium source, respectively, the  $\text{Ni}_2\text{P}/\text{MoO}_x/\text{NF}$  and  $\text{NiSe}_2/\text{MoO}_x/\text{NF}$  can be obtained after treating at the temperature of 350 °C and 400 °C for 2 h, respectively.

Other details of materials characterization and electrochemical measurements were provided in [Supporting Information \(SI\)](#).

## 3. Results and discussion

### 3.1. DFT calculations

To comprehend the profound impact of engineering heterointerfaces between  $\text{Ni}_2\text{P}$  and  $\text{NiSe}_2$  ( $\text{Ni}_2\text{P}-\text{NiSe}_2$ ) and their synergistic coupling with  $\text{MoO}_2$  ( $\text{Ni}_2\text{P}-\text{NiSe}_2/\text{MoO}_2$ ), we initiated our investigation with density functional theory (DFT) calculations. In general, the alkaline HER pathway encompasses the dissociation of  $\text{H}_2\text{O}$  and the formation of adsorbed hydrogen intermediates *via* the Volmer step, ultimately leading to hydrogen generation. Hence, the adsorption and dissociation of water, along with the adsorption of hydrogen, are pivotal steps that fundamentally govern the alkaline HER activity. The atomic models, accompanied by the charge density difference at the  $\text{Ni}_2\text{P}-\text{NiSe}_2$  interface, are elucidated in [Fig. 1a](#). A conspicuous increase in localized charge density at the interface of  $\text{Ni}_2\text{P}-\text{NiSe}_2$  is readily discernible, signifying robust interface electronic interactions. The blue regions signify charge accumulation, while the yellow areas depict charge depletion. Furthermore, we estimated the electrostatic potential along the Z axis to assess the intrinsic potential of  $\text{Ni}_2\text{P}-\text{NiSe}_2$  heterostructure, as presented in [Fig. S1a](#). The corresponding curve demonstrates a charge transfer from the  $\text{Ni}_2\text{P}$  side to the  $\text{NiSe}_2$  component, further highlighting

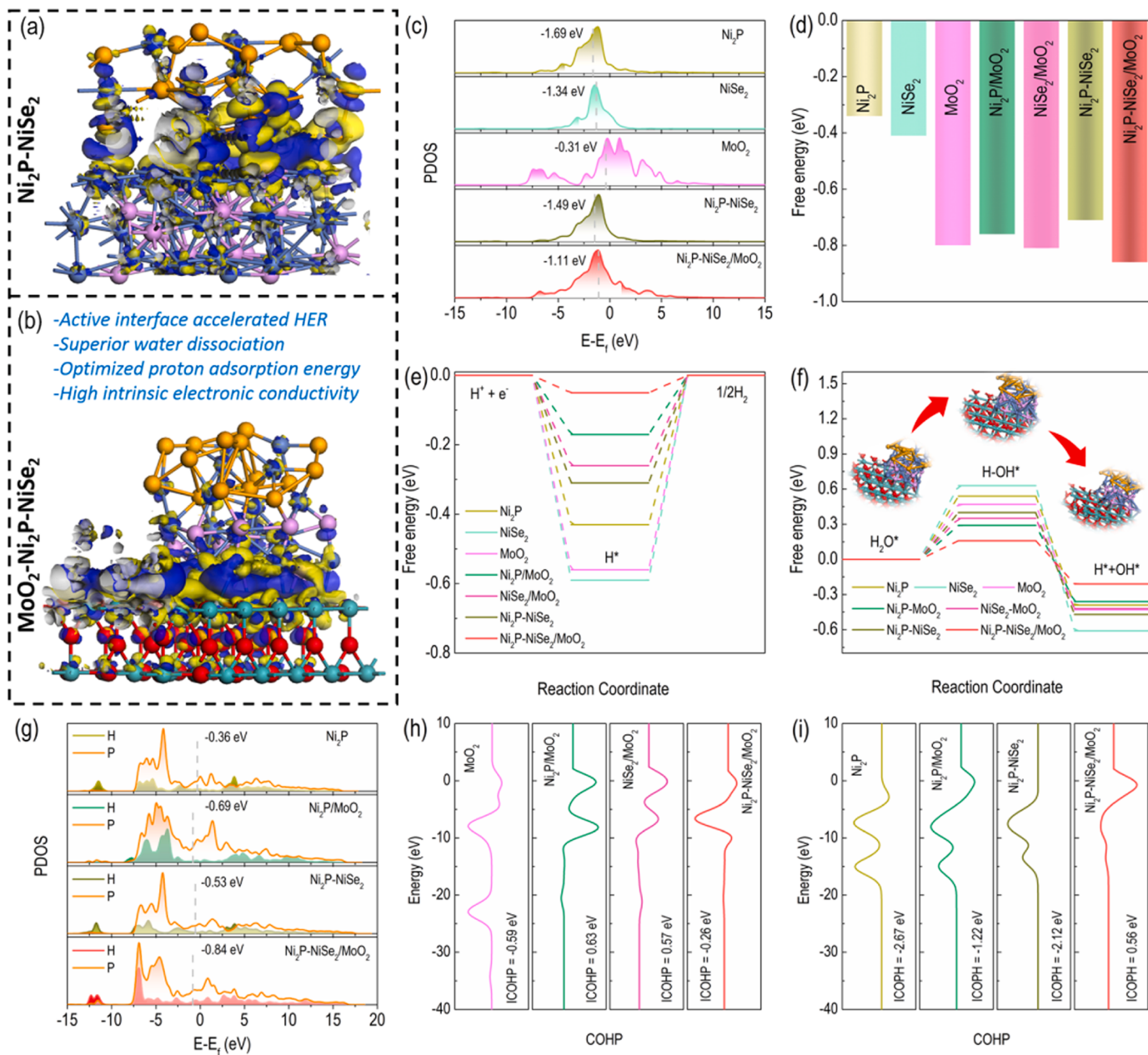


**Fig. 1.** Atomic models with charge density difference plot of  $\text{Ni}_2\text{P}-\text{NiSe}_2$  (a) and  $\text{Ni}_2\text{P}-\text{NiSe}_2/\text{MoO}_2$  (b). The blue and yellow regions represent positive and negative charges, respectively. (c) PDOS for  $\text{Ni}_2\text{P}$ ,  $\text{NiSe}_2$ ,  $\text{MoO}_2$ ,  $\text{Ni}_2\text{P}-\text{NiSe}_2$ ,  $\text{Ni}_2\text{P}-\text{NiSe}_2/\text{MoO}_2$ . (d) Water adsorption energy, (e)  $\Delta G_{\text{H}^*}$  diagram, and (f) Reaction energy diagram of water dissociation on different electrocatalysts. Inset of (f) is the optimized structure models of the adopted adsorption sites of  $\text{H}_2\text{O}^*$ ,  $\text{H}-\text{OH}^*$ , and  $\text{H}^*+\text{OH}^*$  on  $\text{Ni}_2\text{P}-\text{NiSe}_2/\text{MoO}_2$ . Ni, P, Se, Mo, O, and H atoms are presented by grey, pink, brown, cyan, red, and white spheres, respectively. (g) PDOS of H 1s in  $\text{H}^*$  adsorbed on  $\text{Ni}_2\text{P}$ ,  $\text{Ni}_2\text{P}/\text{MoO}_2$ ,  $\text{Ni}_2\text{P}-\text{NiSe}_2$ , and  $\text{Ni}_2\text{P}-\text{NiSe}_2/\text{MoO}_2$ . (h) COHP of active Mo atom and adsorbed O atom for  $\text{MoO}_2$ ,  $\text{Ni}_2\text{P}/\text{MoO}_2$ ,  $\text{NiSe}_2/\text{MoO}_2$ , and  $\text{Ni}_2\text{P}-\text{NiSe}_2/\text{MoO}_2$ . (i) COHP of active P atom and adsorbed  $\text{H}^*$  adsorbed on  $\text{Ni}_2\text{P}$ ,  $\text{Ni}_2\text{P}/\text{MoO}_2$ ,  $\text{Ni}_2\text{P}-\text{NiSe}_2$ , and  $\text{Ni}_2\text{P}-\text{NiSe}_2/\text{MoO}_2$ .

the interfacial electronic interaction's influence. This interaction has the capability to modulate the position of  $d$ -band center ( $\epsilon_d$ ), thereby finely tuning the adsorption of reaction intermediates. This adjustment is evident in the projected density of states (PDOS) shown in Fig. 1c. Fig. 1c illustrates that  $\epsilon_d$  values for  $\text{Ni}_2\text{P}$  and  $\text{NiSe}_2$  are  $-1.69$  and  $-1.34$  eV, respectively, suggesting either excessively weak or strong adsorption characteristics for reaction intermediates. Conversely,  $\text{Ni}_2\text{P}-\text{NiSe}_2$ , with a moderate  $\epsilon_d$  value of  $-1.49$  eV, appears well-suited for optimizing the adsorption of hydrogen and oxygen intermediates, thereby enhancing electrocatalytic activity. Given that  $\text{H}_2\text{O}$  adsorption serves as the initial step in alkaline HER, it is essential to scrutinize the interaction behavior of  $\text{H}_2\text{O}$  on the catalyst surface. The calculated  $\text{H}_2\text{O}$ -adsorption free energy ( $\Delta G_{\text{H}_2\text{O}}$ ) for  $\text{Ni}_2\text{P}-\text{NiSe}_2$ , as illustrated in Fig. 1d, is  $-0.71$  eV. This

value is notably lower than that of the individual  $\text{Ni}_2\text{P}$  and  $\text{NiSe}_2$  components, underscoring that heterointerface engineering effectively promotes  $\text{H}_2\text{O}$  adsorption. This enhancement in  $\text{H}_2\text{O}$  adsorption, in turn, facilitates reactant attraction, thereby expediting the subsequent  $\text{H}_2\text{O}$  cleavage step [22].

The Gibbs free energy of hydrogen ( $\Delta G_{\text{H}^*}$ ) on the catalyst surface is a pivotal factor in the assessment of HER activity. Ideally, HER catalysts should possess a  $\Delta G_{\text{H}^*}$  value close to zero, as this promotes more facile hydrogen adsorption and desorption throughout the entire HER process [23]. Consequently, we systematically evaluated all possible adsorption sites to compare their  $\Delta G_{\text{H}^*}$  values. As depicted in Fig. 1e,  $\Delta G_{\text{H}^*}$  value at the  $\text{Ni}_2\text{P}-\text{NiSe}_2$  interface on the P site ( $-0.31$  eV) significantly approaches the optimal value when compared to the individual  $\text{Ni}_2\text{P}$

( $-0.43$  eV) and  $\text{NiSe}_2$  ( $-0.59$  eV) components. This observation underscores that the interface interaction between  $\text{Ni}_2\text{P}$  and  $\text{NiSe}_2$  optimizes hydrogen adsorption, thereby contributing to higher intrinsic HER activity. Considering of the higher electronegativity of Se (2.55) in comparison to P (2.19), Se atoms nearby  $\text{Ni}_2\text{P}$ - $\text{NiSe}_2$  interface would be more likely to attract electrons from adjacent P atoms, thereby resulting in the redistribution for surface charge density, which is further corroborated by the distorted charge density at the interface region in Fig. 1a. As for  $\text{Ni}_2\text{P}$ - $\text{NiSe}_2$  interface, electrons surrounding P atoms conspicuously transfer to adjacent Se sites, leading to a charge depletion region around P sites, so that a moderate  $\Delta G_{\text{H}^*}$  value on P sites is achieved [24,25]. Furthermore, we calculated the energy barrier for  $\text{H}_2\text{O}$  dissociation, as presented in Fig. 1f. The energy barriers for  $\text{H}_2\text{O}$  dissociation are determined to be 0.54, 0.63, and 0.40 eV for  $\text{Ni}_2\text{P}$ ,  $\text{NiSe}_2$ , and  $\text{Ni}_2\text{P}$ - $\text{NiSe}_2$ , respectively. This energy difference demonstrates that the construction of the  $\text{Ni}_2\text{P}$ - $\text{NiSe}_2$  interface predominantly facilitates the cleavage of the HO-H bond, thereby increasing the concentration of  $\text{H}^*$  at active sites. Consequently, this enhancement significantly accelerates alkaline HER kinetics on  $\text{Ni}_2\text{P}$ - $\text{NiSe}_2$  interface.

On the other hand, these findings of theoretical calculations lead us to wonder whether these adsorption energy of intermediates and reaction energy barrier for  $\text{Ni}_2\text{P}$ - $\text{NiSe}_2$  can be further optimized for exceptional performance. To this end, we introduced an interface-rich architecture by anchoring  $\text{Ni}_2\text{P}$ - $\text{NiSe}_2$  onto a  $\text{MoO}_2$  substrate ( $\text{Ni}_2\text{P}$ - $\text{NiSe}_2$ / $\text{MoO}_2$ ) to further fine-tune the electronic configuration and create additional active sites. Notably, we observed electron redistribution between  $\text{MoO}_2$  and  $\text{Ni}_2\text{P}$ - $\text{NiSe}_2$  at the interface (Fig. 1b), with electrons transferring from  $\text{MoO}_2$  to  $\text{Ni}_2\text{P}$ - $\text{NiSe}_2$  (Fig. S1b). According to the density of states (DOS) in Fig. S2, it is evident that the  $\text{Ni}_2\text{P}$ - $\text{NiSe}_2$ / $\text{MoO}_2$  heterostructures exhibit a notably elevated electron density at the Fermi level when compared with  $\text{Ni}_2\text{P}$ ,  $\text{NiSe}_2$ , and  $\text{Ni}_2\text{P}$ - $\text{NiSe}_2$  components. This observation indicates the presence of synergistically coupled electron orbitals at the interface of the  $\text{Ni}_2\text{P}$ - $\text{NiSe}_2$ / $\text{MoO}_2$  heterostructure. Such coupling optimizes the conductivity of the composite material and concurrently mitigates the charge transfer resistance. The discerned optimization in conductivity and reduction in charge transfer resistance are anticipated to confer beneficial attributes to the electrocatalytic processes facilitated by  $\text{Ni}_2\text{P}$ - $\text{NiSe}_2$ / $\text{MoO}_2$ . This redistribution, coupled with the multiple-interface construction, further fine-tunes the position of  $\varepsilon_d$ , thereby tailoring the adsorption characteristics of reaction intermediates. Moreover, the introduction of  $\text{MoO}_2$  leads to a shift in the  $\Delta G_{\text{H}_2\text{O}}$  value from  $-0.71$  eV in  $\text{Ni}_2\text{P}$ - $\text{NiSe}_2$  to  $-0.86$  eV (Fig. 1d), indicating that the electron-deficient Mo sites exhibit favorable energy levels for water adsorption. Additionally, the  $\Delta G_{\text{H}^*}$  value for  $\text{Ni}_2\text{P}$ - $\text{NiSe}_2$ / $\text{MoO}_2$  on the P site is  $-0.05$  eV (Fig. 1e), lower than that of  $\text{Ni}_2\text{P}$ - $\text{NiSe}_2$ , implying the more optimized adsorption behavior after  $\text{MoO}_2$  introduction. Most notably, the energy barrier for  $\text{H}_2\text{O}$  dissociation in the  $\text{Ni}_2\text{P}$ - $\text{NiSe}_2$ / $\text{MoO}_2$  structure decreases to 0.16 eV (Fig. 1f), indicating that the coupling of  $\text{MoO}_2$  with the  $\text{Ni}_2\text{P}$ - $\text{NiSe}_2$  interface further facilitates the cleavage of HO-H bonds. In the  $\text{Ni}_2\text{P}$ - $\text{NiSe}_2$ / $\text{MoO}_2$  structure, the positively charged  $\text{MoO}_2$  surface promotes the adsorption of electron-rich oxygen atoms in  $\text{H}_2\text{O}$ , activating the  $\text{H}_2\text{O}$  molecule and rendering it more amenable to splitting on  $\text{MoO}_2$ . This synergistic effect between  $\text{MoO}_2$  and the  $\text{Ni}_2\text{P}$ - $\text{NiSe}_2$  interface contributes to the overall enhancement in catalytic performance.

To gain deeper insights into the exceptional catalytic activity of  $\text{Ni}_2\text{P}$ - $\text{NiSe}_2$ / $\text{MoO}_2$ , we conducted an in-depth investigation into its electronic structure. We initially confirmed the electronic band structure modulation resulting from the coupling of  $\text{Ni}_2\text{P}$ - $\text{NiSe}_2$  with  $\text{MoO}_2$  through the analysis of the PDOS of active P and H atoms (Fig. 1g). This analysis reveals a downshift in the H 1s-band center to a lower energy value ( $-0.84$  eV) in  $\text{Ni}_2\text{P}$ - $\text{NiSe}_2$ / $\text{MoO}_2$ , compared to  $\text{Ni}_2\text{P}$ / $\text{MoO}_2$  ( $-0.69$  eV),  $\text{Ni}_2\text{P}$ - $\text{NiSe}_2$  ( $-0.53$  eV), and  $\text{Ni}_2\text{P}$  ( $-0.36$  eV). This downshift indicates a reduction in the binding strength of  $\text{H}^*$  and implies the smoother release of  $\text{H}^*$  from the P site of  $\text{Ni}_2\text{P}$ - $\text{NiSe}_2$ / $\text{MoO}_2$ . To further elucidate the bonding interactions, we employed crystal orbital Hamilton population

(COHP) calculations for the active site [26]. In the COHP diagram, positive and negative values correspond to bonding and antibonding contributions, respectively. The integrated-COHP (ICOHP) value for Mo and the adsorbed oxygen atom in  $\text{H}_2\text{O}$  is found to be  $-0.26$  eV for  $\text{Ni}_2\text{P}$ - $\text{NiSe}_2$ / $\text{MoO}_2$  (Fig. 1h), which is lower than that of bare  $\text{MoO}_2$ ,  $\text{Ni}_2\text{P}$ / $\text{MoO}_2$ , and  $\text{NiSe}_2$ / $\text{MoO}_2$ . This observation indicates a stronger bonding interaction between the active-surface Mo and adsorbed  $\text{H}_2\text{O}$  on the  $\text{Ni}_2\text{P}$ - $\text{NiSe}_2$ / $\text{MoO}_2$  surface. Consequently, water molecules can be captured at a faster rate, facilitating the Volmer reaction on the  $\text{Ni}_2\text{P}$ - $\text{NiSe}_2$ / $\text{MoO}_2$  surface. Additionally, COHP and ICOHP calculations (Fig. 1i) reveal that the P sites in  $\text{Ni}_2\text{P}$ - $\text{NiSe}_2$ / $\text{MoO}_2$  substantially decreases the occupancy rate of the P-H bonding state compared to  $\text{Ni}_2\text{P}$ / $\text{MoO}_2$ ,  $\text{Ni}_2\text{P}$ - $\text{NiSe}_2$ , and  $\text{Ni}_2\text{P}$ . This reduction in occupancy is beneficial for desorption of hydrogen, contributing to a higher HER activity.

Overall, in this integrated  $\text{Ni}_2\text{P}$ - $\text{NiSe}_2$ / $\text{MoO}_2$  system, the electronic interaction between  $\text{Ni}_2\text{P}$ - $\text{NiSe}_2$  and  $\text{MoO}_2$  can synergistically facilitate  $\text{H}_2\text{O}$  adsorption, accelerate  $\text{H}_2\text{O}$  dissociation and effectively adsorb produced  $\text{H}^*$ , thereby evidently boosting each reaction steps involved in alkaline HER process according to DFT calculation.

### 3.2. Catalyst synthesis and characterization

In response to theoretical predictions, as schematically illustrated in Fig. 2a, a facile methodology is developed to engineer interface-rich  $\text{Ni}_2\text{P}$ - $\text{NiSe}_2$  nanoparticles firmly affixed to amorphous  $\text{MoO}_x$  nanorods on nickel foam. Initially, the  $\text{NiMoO}_4\text{-xH}_2\text{O}$  nanorods on conductive nickel foam (denoted as  $\text{Ni}$ - $\text{Mo}$ - $\text{O}$ / $\text{NF}$ ) are achieved via a hydrothermal process, yielding one-dimensional nanorods with diameters in the range of 50 to 100 nm, as verified through SEM and TEM images (Fig. S3). X-ray powder diffraction (XRD) pattern (Fig. S4) of  $\text{Ni}$ - $\text{Mo}$ - $\text{O}$ / $\text{NF}$  confirms the crystalline nature of the  $\text{NiMoO}_4\text{-xH}_2\text{O}$  phase (JCPDS No.13-0128) [27]. Subsequently,  $\text{NiMoO}_4\text{-xH}_2\text{O}$  is annealed under the reductive atmosphere of 10%  $\text{H}_2$ /Ar, resulting in the formation of distinctive rod-like structures comprising numerous nanoparticles (denoted as  $\text{Ni}$ - $\text{MoO}_x$ / $\text{NF}$ ). XRD pattern (Fig. S4) exclusively exhibits the presence of a single Ni phase (JCPDS No.04-0850) [28], with no discernible crystalline Mo-based oxides, agreeing with the observations reported previously [29]. The uniform one-dimensional nanorod morphology is faithfully retained by  $\text{Ni}$ - $\text{MoO}_x$ / $\text{NF}$ , as evidenced by SEM image (Fig. S5a). TEM observations (Fig. S5b,c) reveal the anchoring of crystalline Ni nanoparticles onto the nanorods possessing an amorphous structure. Detailed STEM and EDX elemental mapping (Fig. S5d-g) further confirm the uniform spatial distribution of Mo and O along the entire length of individual nanorods, with Ni exclusively localized within the nanoparticle regions. Furthermore, X-ray photoelectron spectroscopy (XPS) investigations (Fig. S6) also proves the formation of  $\text{Ni}^0$  and  $\text{Mo}^{4+}$  species.

Ultimately, employing the conventional phosphoselenization procedure, the interface-enriched  $\text{Ni}_2\text{P}$ - $\text{NiSe}_2$  nanoparticles are successfully integrated with  $\text{MoO}_x$  nanorods, yielding  $\text{Ni}_2\text{P}$ - $\text{NiSe}_2$ / $\text{MoO}_x$  heterostructures on nickel foam (denoted as  $\text{Ni}_2\text{P}$ - $\text{NiSe}_2$ / $\text{MoO}_x$ / $\text{NF}$ ). The typical SEM image (Fig. 2b-d) and TEM image (Fig. 2e) of  $\text{Ni}_2\text{P}$ - $\text{NiSe}_2$ / $\text{MoO}_x$ / $\text{NF}$  exhibit the nanorod arrays with an abundance of minute nanoparticles distributed across their surfaces, offering a greater number of readily accessible active sites for electrochemical reactions. High-resolution TEM images (Fig. 2f,g) affirm the generation of numerous interfaces between the (210) planes of  $\text{Ni}_2\text{P}$  and  $\text{NiSe}_2$ , firmly anchored onto the amorphous nanorods, which are consistent with their selected-area electron diffraction (SAED) pattern (Fig. 2e). Besides, elemental distribution analysis through energy dispersive X-ray spectroscopy (EDX) mapping images (Fig. 2h) reveal the uniform dispersion of Mo, O, Ni, P, and Se elements across the entire length of the nanorods, while the Ni element formed dispersive nanoparticles are still observed.

The distinctive diffraction patterns are presented on XRD patterns to identify the phase structure of catalysts (Fig. 3a). In the case of  $\text{Ni}_2\text{P}$ -

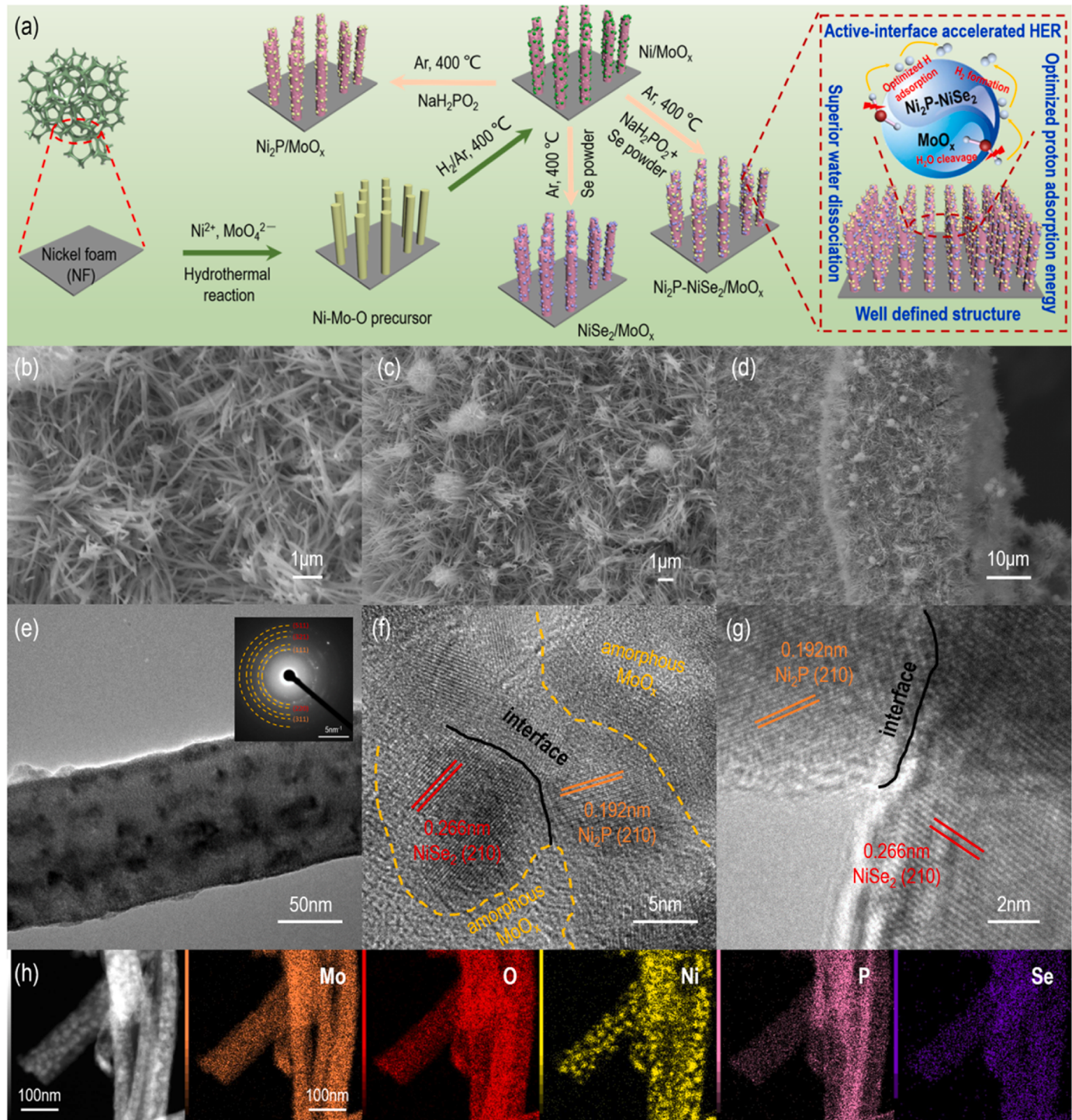


**Fig. 2.** (a) Schematic illustration of the fabrication of  $\text{Ni}_2\text{P-NiSe}_2/\text{MoO}_x/\text{NF}$ . (b-d) SEM, (e) TEM, (f,g) High-resolution TEM images of  $\text{Ni}_2\text{P-NiSe}_2/\text{MoO}_x/\text{NF}$ . Inset of (e) is the SAED pattern. (h) STEM images and the corresponding EDX elemental mapping of  $\text{Ni}_2\text{P-NiSe}_2/\text{MoO}_x/\text{NF}$ .

$\text{NiSe}_2/\text{MoO}_x/\text{NF}$ , the discernible peaks located at  $40.8^\circ$ ,  $44.6^\circ$ ,  $47.3^\circ$ , and  $54.2^\circ$  ( $2\theta$ ) correspond to the (111), (201), (210), and (300) planes of  $\text{Ni}_2\text{P}$  (JCPDS No. 03-0953) [30]. Furthermore, the peaks at  $33.6^\circ$ ,  $36.9^\circ$ ,  $50.7^\circ$ ,  $55.5^\circ$ , and  $57.8^\circ$  ( $2\theta$ ) are indexed to the (210), (211), (311), (023), and (321) planes of  $\text{NiSe}_2$  (JCPDS No. 65-5016) [31]. Additionally, XRD patterns of  $\text{Ni}_2\text{P}/\text{MoO}_x/\text{NF}$  and  $\text{NiSe}_2/\text{MoO}_x/\text{NF}$  exclusively reveal discernible peaks associated with  $\text{Ni}_2\text{P}$  and  $\text{NiSe}_2$  phases, respectively. Notably, across all prepared samples, no discernible diffraction peaks attributed to molybdenum-based constituents are observed, which is consistent with their TEM observations, thus

providing complementary evidence for the crystalline-amorphous nature of the fabricated  $\text{Ni}_2\text{P-NiSe}_2/\text{MoO}_x$  heterostructures. In contrast to the standard diffraction patterns of pristine  $\text{Ni}_2\text{P}$  or  $\text{NiSe}_2$ , the relatively poor diffraction peak intensities in  $\text{Ni}_2\text{P-NiSe}_2/\text{MoO}_x/\text{NF}$  sample can be attributed to the diminutive particle size of the formed  $\text{Ni}_2\text{P-NiSe}_2$  heterostructures. Combined XRD, TEM, high-resolution TEM, and EDX results of  $\text{Ni}_2\text{P-NiSe}_2/\text{MoO}_x/\text{NF}$  conclusively reveal the successful synthesis of heterostructures but not simply recombination of  $\text{Ni}_2\text{P}$  and  $\text{NiSe}_2$  components. Detailed characterizations of other samples, including  $\text{Ni}_2\text{P}/\text{MoO}_x/\text{NF}$  (Fig. S7),  $\text{NiSe}_2/\text{MoO}_x/\text{NF}$  (Fig. S8), and

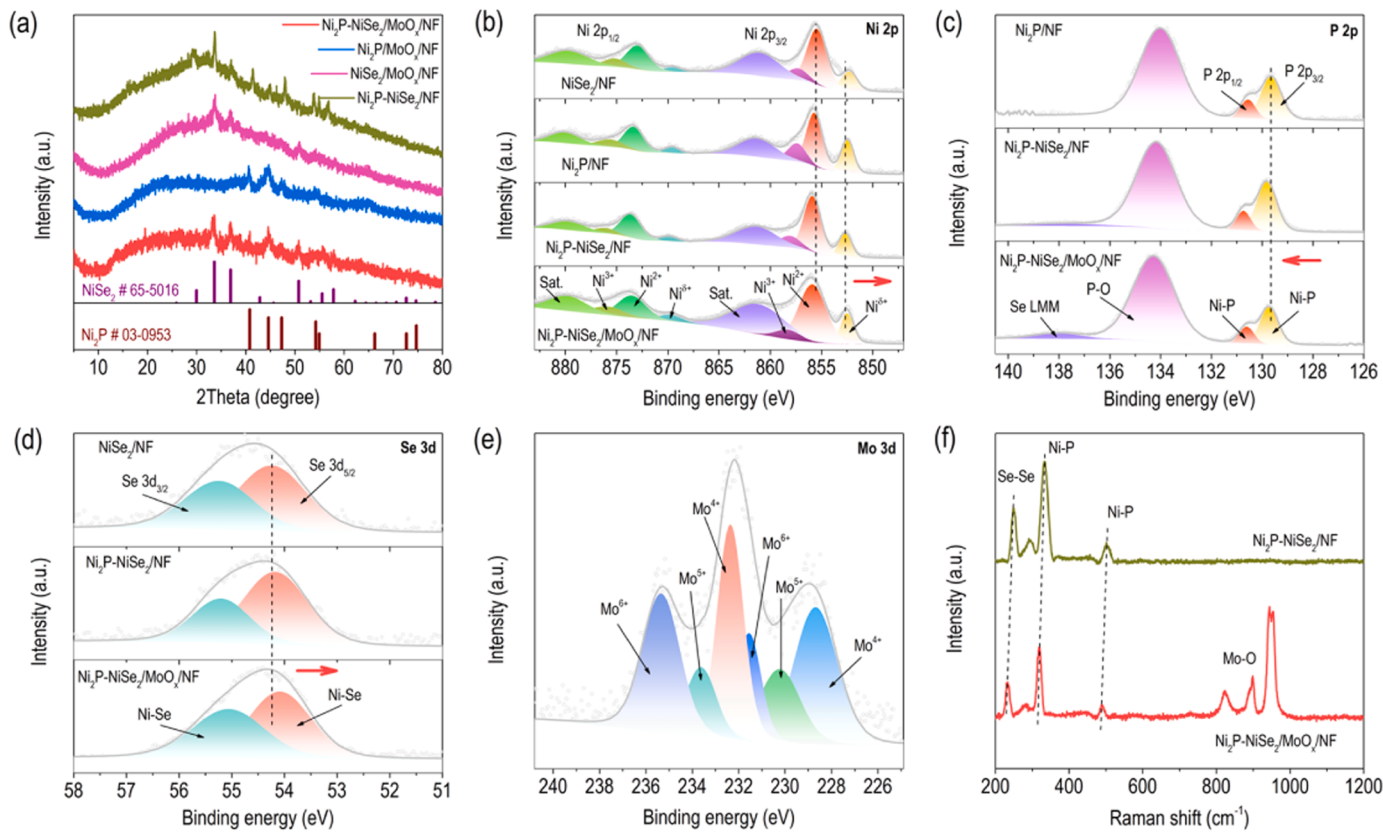


**Fig. 3.** (a) XRD pattern of  $\text{Ni}_2\text{P}-\text{NiSe}_2/\text{MoO}_x/\text{NF}$ ,  $\text{Ni}_2\text{P}/\text{MoO}_x/\text{NF}$ ,  $\text{NiSe}_2/\text{MoO}_x/\text{NF}$ , and  $\text{Ni}_2\text{P}-\text{NiSe}_2/\text{NF}$ . High-resolution XPS spectra of the Ni 2p (b), P 2p (c), Se 2p (d), and Mo 3d (e) for  $\text{Ni}_2\text{P}-\text{NiSe}_2/\text{MoO}_x/\text{NF}$ ,  $\text{Ni}_2\text{P}-\text{NiSe}_2/\text{NF}$ ,  $\text{Ni}_2\text{P}/\text{NF}$ , and  $\text{NiSe}_2/\text{NF}$ . (f) Raman spectra of  $\text{Ni}_2\text{P}-\text{NiSe}_2/\text{MoO}_x/\text{NF}$  and  $\text{Ni}_2\text{P}-\text{NiSe}_2/\text{NF}$ .

$\text{Ni}_2\text{P}-\text{NiSe}_2/\text{NF}$  (Fig. S9), are provided, and the corresponding results also affirm the formation of the required structure and compositions. The  $\text{N}_2$  adsorption-desorption analysis (Fig. S10) exhibits the larger specific surface area of the prepared samples, indicating the porous structure, well consistent with the SEM and TEM observations.

Surface chemical composition and electron interactions within the catalysts are investigated by XPS. To eliminate contributions from the nickel foam substrate, all XPS analyses were conducted on powder samples obtained by ultrasonication from the nickel foam substrate. The XPS survey spectra in Fig. S11a display the presence of targeted elements including Mo, O, Ni, P, and Se in  $\text{Ni}_2\text{P}-\text{NiSe}_2/\text{MoO}_x/\text{NF}$ . In the high-resolution Ni 2p spectrum (Fig. 3b) of  $\text{Ni}_2\text{P}-\text{NiSe}_2/\text{MoO}_x/\text{NF}$ , distinct peaks at 852.5 and 869.7 eV are attributed to  $\text{Ni}^{\delta+}$  ( $0 < \delta < 2$ ), corresponding to  $\text{Ni-P}/\text{Se}$  bonding [32]. Concurrently, the presence of surface-oxidized  $\text{Ni}^{2+}/\text{Ni}^{3+}$  species is observed, likely a consequence of inevitable air exposure. The P 2p spectrum (Fig. 3c) of  $\text{Ni}_2\text{P}-\text{NiSe}_2/\text{MoO}_x/\text{NF}$  reveals two double peaks at 129.7 and 130.6 eV, indicative of  $\text{Ni-P}$  bonds [33]. Notably, these peaks exhibit a slight upward shift of 0.2 eV relative to those observed in pure  $\text{Ni}_2\text{P}/\text{NF}$ . Conversely, the Se 2p spectrum (Fig. 3d) of  $\text{Ni}_2\text{P}-\text{NiSe}_2/\text{MoO}_x/\text{NF}$  displays two peaks at 54.1 and 55.1 eV, assigned to  $\text{Ni-Se}$  species [34]. These binding energies exhibit a negative shift of approximately 0.3 eV when compared to pure  $\text{NiSe}_2/\text{NF}$ . Similar shifts in binding energies are observed for the  $\text{Ni}_2\text{P}-\text{NiSe}_2/\text{NF}$  sample. These findings indicate the establishment of robust internal electron interactions and redistribution within the heterostructures, where electrons transfer from P to Se at the  $\text{Ni}_2\text{P}-\text{NiSe}_2$  heterointerfaces. In the Mo 3d region of  $\text{Ni}_2\text{P}-\text{NiSe}_2/\text{MoO}_x/\text{NF}$  (Fig. 3e), peaks centered at 228.7 and 232.4 eV correspond to  $\text{Mo}^{4+}$ , indicative of the presence of  $\text{MoO}_2$  [35,36]. Another pair of peaks are attributed to  $\text{Mo}^{5+}$  and  $\text{Mo}^{6+}$ , respectively. A comparison of the  $\text{Ni}^{\delta+}$  peaks in  $\text{Ni}_2\text{P}-\text{NiSe}_2/\text{MoO}_x/\text{NF}$  and  $\text{Ni}_2\text{P}-\text{NiSe}_2/\text{NF}$  reveals a minor negative shift in the binding energies of  $\text{Ni}_2\text{P}-\text{NiSe}_2/\text{MoO}_x/\text{NF}$ , suggesting an

enrichment of electron density at the interfacial Ni atoms. This shift is likely attributed to electron transfer from the  $\text{MoO}_x$  substrate to  $\text{Ni}_2\text{P}-\text{NiSe}_2$ , further highlighting the intricate electron interactions within the heterostructure.

Furthermore, Raman spectra were employed to gain insights into the vibrational properties of the catalysts. Among typical pyrite-structure compounds, two characteristic peaks are commonly observed, corresponding to  $\text{X}_2$  (Se, P) librational ( $\text{E}_g$ ) and phase stretch ( $\text{A}_g$ ) modes associated with the X-X dumbbells [37]. As depicted in Fig. 3f, a prominent peak at  $232.7 \text{ cm}^{-1}$  can be unequivocally attributed to the Se-Se stretching mode of cubic  $\text{NiSe}_2$ , while two peaks at  $320.1$  and  $488.4 \text{ cm}^{-1}$  are typically associated with  $\text{NiP}_2$  [38,39]. Additionally, peaks located at  $822.1$ ,  $898.4$ , and  $946.8 \text{ cm}^{-1}$  are identified as the Mo-O bond vibration modes characteristic of the monoclinic-phase  $\text{MoO}_2$  [40]. Notably, a comparison between  $\text{Ni}_2\text{P}-\text{NiSe}_2/\text{NF}$  and  $\text{Ni}_2\text{P}-\text{NiSe}_2/\text{MoO}_x/\text{NF}$  reveals a slight negative shift in the  $\text{Ni-P}/\text{Ni-Se}$  bonds. This observation suggests the presence of robust electron interactions between  $\text{MoO}_x$  and  $\text{Ni}_2\text{P}-\text{NiSe}_2$ . Consequently, it indicates the occurrence of pronounced localized charge redistribution and charge transfer at the interface of  $\text{Ni}_2\text{P}-\text{NiSe}_2/\text{MoO}_x$ , consistent with theoretical predictions, which is expected to synergistically function together and obtain exceptional alkaline electrochemical performance.

### 3.3. HER and OER catalytic performance

Motivated by the promising theoretical predictions and the sophisticated interface architecture of the developed  $\text{Ni}_2\text{P}-\text{NiSe}_2/\text{MoO}_x/\text{NF}$  catalyst, we systematically assessed its electrocatalytic performance for HER in  $\text{H}_2$ -saturated 1.0 M KOH, employing a conventional three-electrode configuration. Before conducting electrochemical measurements, the reference electrode of  $\text{Hg}/\text{HgO}$  was meticulously calibrated to the reversible hydrogen electrode (RHE) (Fig. S12). The  $iR$ -

compensated polarization curves in Fig. 4a unequivocally demonstrate the substantially improved HER activities of the electrocatalysts after heterostructure engineering. The activity trend follows the order of  $\text{Ni}_2\text{P}-\text{NiSe}_2/\text{MoO}_x/\text{NF} > \text{Pt/C/NF}$  (with optimized 20% Pt/C loading of  $4.0 \text{ mg cm}^{-2}$ , Fig. S13)  $> \text{Ni}_2\text{P}/\text{MoO}_x/\text{NF} > \text{NiSe}_2/\text{MoO}_x/\text{NF} > \text{Ni}_2\text{P}-\text{NiSe}_2/\text{NF} > \text{Ni}_2\text{P}/\text{NF} > \text{NiSe}_2/\text{NF} > \text{NF}$ . Remarkably, the introduction of  $\text{MoO}_x$  species to construct heterostructures leads to a significant enhancement in the electrocatalytic activities of the resulting catalysts. For instance,  $\text{Ni}_2\text{P}/\text{MoO}_x/\text{NF}$  and  $\text{NiSe}_2/\text{MoO}_x/\text{NF}$  require overpotentials of 61 and 84 mV, respectively, to achieve a current density of  $10 \text{ mA cm}^{-2}$ , which are notably lower than those observed for  $\text{Ni}_2\text{P}/\text{NF}$  (153 mV) and  $\text{NiSe}_2/\text{NF}$  (184 mV). Notably,  $\text{Ni}_2\text{P}-\text{NiSe}_2/\text{NF}$  catalyst necessitates overpotentials of 119, 271, and 428 mV at current densities of 10, 100, and  $500 \text{ mA cm}^{-2}$ , respectively. However, after coupling

with  $\text{MoO}_x$  substrates, the resultant  $\text{Ni}_2\text{P}-\text{NiSe}_2/\text{MoO}_x/\text{NF}$  only needs the overpotential of 23, 96, and 263 mV at 10, 100, and  $500 \text{ mA cm}^{-2}$ , respectively. This performance surpasses even the widely acclaimed  $\text{Pt/C/NF}$  catalysts (Fig. S14), delivering the exceptional alkaline HER activity achieved through the synergistic interaction between interface-rich  $\text{Ni}_2\text{P}-\text{NiSe}_2$  and amorphous  $\text{MoO}_x$  substrates. Impressively, the alkaline HER activity of this interface-rich  $\text{Ni}_2\text{P}-\text{NiSe}_2/\text{MoO}_x/\text{NF}$  is comparable and even superior to most recently reported phosphide- and selenide-based HER electrocatalysts (Fig. S15, Table S1). Moreover, to attain the industrially meaningful current density of  $1000 \text{ mA cm}^{-2}$ ,  $\text{Ni}_2\text{P}-\text{NiSe}_2/\text{MoO}_x/\text{NF}$  requires an overpotential of 424 mV, which is lower than that of  $\text{Pt/C/NF}$  (501 mV), demonstrating the substantial practical potential of this catalyst in industrially relevant applications.

As revealed by the Tafel plots in Fig. 4b,  $\text{Ni}_2\text{P}-\text{NiSe}_2/\text{MoO}_x/\text{NF}$

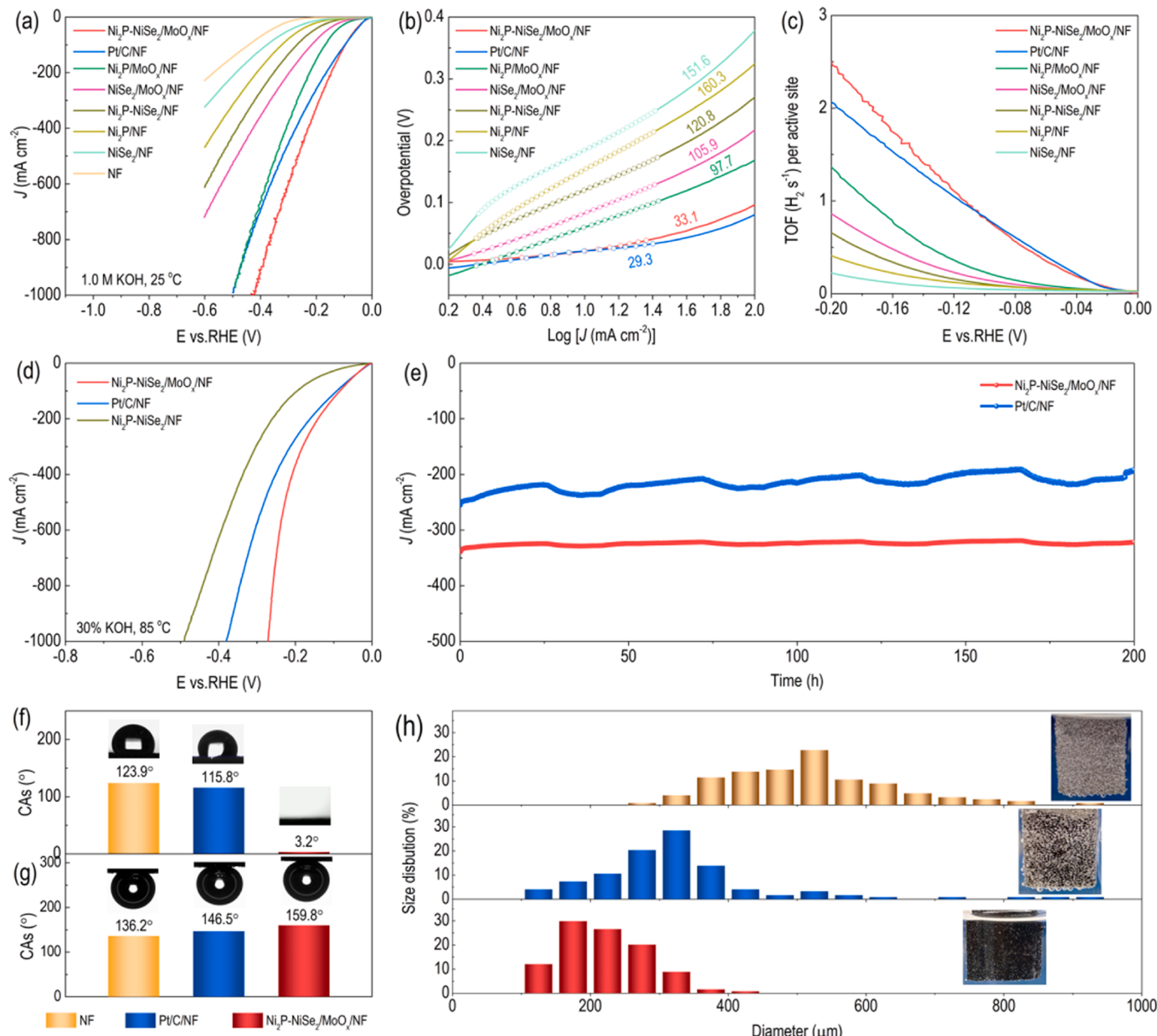


**Fig. 4.** Electrochemical HER performance of catalysts in  $\text{H}_2$ -saturated 1.0 M KOH. (a) iR-corrected LSV curves measured in 1.0 M KOH + 25 °C. (b) Tafel plots. (c) Comparison of TOF values of different electrocatalysts for HER. (d) iR-corrected LSV curves measured in 30% KOH + 85 °C. (e) Electrochemical durability test of  $\text{Ni}_2\text{P}-\text{NiSe}_2/\text{MoO}_x/\text{NF}$  and  $\text{Pt/C/NF}$  measured by chronoamperometry tests at  $-0.20 \text{ V}$  vs. RHE. Mass transport measurements. Water CAs (f) and bubble CAs (g) for bare NF, Pt/C/NF, and  $\text{Ni}_2\text{P}-\text{NiSe}_2/\text{MoO}_x/\text{NF}$ . (h) Size distributions of  $\text{H}_2$  bubbles on the surface of catalysts, the photograph (inset) shows sharp contrast during the release of gas bubbles on the surfaces for bare NF, Pt/C/NF, and  $\text{Ni}_2\text{P}-\text{NiSe}_2/\text{MoO}_x/\text{NF}$ .

exhibits the lowest Tafel slope of  $33.1 \text{ mV dec}^{-1}$ , in comparison to the other samples, verifying the significantly improved HER kinetics though Volmer-Heyrovsky mechanism. Moreover, the reduced Tafel slope of  $\text{Ni}_2\text{P}-\text{NiSe}_2/\text{MoO}_x/\text{NF}$  relative to  $\text{Ni}_2\text{P}-\text{NiSe}_2/\text{NF}$  indicates an accelerated  $\text{H}_2\text{O}$  dissociation step (Volmer reaction) at the interface-rich reaction sites. This finding is consistent with the theoretical prediction that the emergence of  $\text{MoO}_x$  to engineer heterostructures would lower the  $\text{H}_2\text{O}$  dissociation energy [41]. Similar trends are observed for the catalytic comparison between  $\text{Ni}_2\text{P}/\text{MoO}_x/\text{NF}$  and  $\text{Ni}_2\text{P}/\text{NF}$ , as well as between  $\text{NiSe}_2/\text{MoO}_x/\text{NF}$  and  $\text{NiSe}_2/\text{NF}$ . This is further corroborated by the larger exchange current densities ( $J_0$ ) observed for  $\text{Ni}_2\text{P}-\text{NiSe}_2/\text{MoO}_x/\text{NF}$  ( $2.15 \text{ mA cm}^{-2}$ ), close to that of  $\text{Pt}/\text{C}/\text{NF}$  catalyst ( $2.21 \text{ mA cm}^{-2}$ ), and superior to that of other samples (Fig. S16). To gain further insights into the synergistic activation of  $\text{H}_2\text{O}$  after adsorption on  $\text{Ni}_2\text{P}-\text{NiSe}_2/\text{MoO}_x/\text{NF}$  and  $\text{Ni}_2\text{P}-\text{NiSe}_2/\text{NF}$ , Fourier-transform infrared spectra with attenuated total reflection (FTIR-ATR) were conducted. As displayed in Fig. S17, a prominent band at  $1639.1 \text{ cm}^{-1}$  is attributed to the H-OH bending vibration of  $\text{H}_2\text{O}$  adsorbed on  $\text{Ni}_2\text{P}-\text{NiSe}_2/\text{NF}$ . A red shift of approximately  $5 \text{ cm}^{-1}$  is observed for  $\text{H}_2\text{O}$  adsorbed on  $\text{Ni}_2\text{P}-\text{NiSe}_2/\text{MoO}_x/\text{NF}$  ( $1634.2 \text{ cm}^{-1}$ ), indicating the elongation of H-OH bonds due to the activation effect. This elongation is conducive to the breaking of H-OH bonds, suggesting enhanced  $\text{H}_2\text{O}$  activation on  $\text{Ni}_2\text{P}-\text{NiSe}_2/\text{MoO}_x/\text{NF}$  catalyst [42].

To experimentally investigate the enhanced reaction kinetics, we calculated the kinetics energy barrier ( $E_a$ ) using the Arrhenius equation. Temperature-dependent polarization curves were obtained for  $\text{Ni}_2\text{P}-\text{NiSe}_2/\text{MoO}_x/\text{NF}$  and  $\text{Ni}_2\text{P}-\text{NiSe}_2/\text{NF}$  over a range of temperatures, specifically at 25, 35, 45, 55, and  $65^\circ\text{C}$ . The HER activities on both catalysts exhibit significant improvements with increasing temperature.  $\text{Ni}_2\text{P}-\text{NiSe}_2/\text{MoO}_x/\text{NF}$  requires  $-10.7 \text{ mV}$  (without  $iR$  compensate) to afford  $10 \text{ mA cm}^{-2}$  at  $65^\circ\text{C}$  (Fig. S18a), which only increases by 194% at the temperature of  $25^\circ\text{C}$  ( $31.5 \text{ mV}$ ), while  $\text{Ni}_2\text{P}-\text{NiSe}_2/\text{NF}$  exhibits 653% increase in overpotential (from  $20.6$  to  $134.6 \text{ mV}$ ) under the identical conditions (Fig. S18b). The linear Arrhenius plots (Fig. S18c) illustrate the lower activation energy ( $E_a$ ) of  $0.25 \text{ kJ mol}^{-1}$  for  $\text{Ni}_2\text{P}-\text{NiSe}_2/\text{MoO}_x/\text{NF}$ , which is lower than that of  $\text{Ni}_2\text{P}-\text{NiSe}_2/\text{NF}$  ( $0.38 \text{ kJ mol}^{-1}$ ), again verifying the existence of  $\text{MoO}_x$  to engineer heterostructures reduce the kinetics energy barrier and accelerates the reaction kinetics for water dissociation.

To further investigate the improved HER performance as well as the intrinsic catalytic ability of electrocatalysts, the electrochemical impedance spectroscopy (EIS) and electrochemical double-layer capacitance ( $C_{dl}$ ) are calculated. As expected,  $\text{Ni}_2\text{P}-\text{NiSe}_2/\text{MoO}_x/\text{NF}$  exhibits the lowest charge-transfer resistance ( $R_{ct}$ ) (Fig. S19) and the highest  $C_{dl}$  (Fig. S20) when compared to other samples. These results manifest superior electron-transfer capability and a higher number of accessible active sites, collectively enhancing the HER activity with faster reaction kinetics. At an overpotential of  $200 \text{ mV}$ ,  $\text{Ni}_2\text{P}-\text{NiSe}_2/\text{MoO}_x/\text{NF}$  achieves a turnover frequency (TOF) of  $2.47 \text{ s}^{-1}$  (Fig. 4c), which is larger than that of  $\text{Pt}/\text{C}/\text{NF}$  as well as other samples, demonstrating the superior intrinsic activity. Furthermore, this higher intrinsic activity is corroborated by the electrochemically active surface area (ECSA)-normalized HER polarization curves (Fig. S22), wherein  $\text{Ni}_2\text{P}-\text{NiSe}_2/\text{MoO}_x/\text{NF}$  still exhibits the positive onset potential and rapidly increasing cathodic current.

Encouraged by the exceptional HER performance,  $\text{Ni}_2\text{P}-\text{NiSe}_2/\text{MoO}_x/\text{NF}$  is further measured in an industrial condition ( $30\%$  KOH,  $85^\circ\text{C}$ ) to assess its practical applicability. In this demanding condition, compared to the larger overpotential of  $\text{Ni}_2\text{P}-\text{NiSe}_2/\text{NF}$  ( $-0.197$ ,  $-0.366$ , and  $-0.489 \text{ V}$ ) and  $\text{Pt}/\text{C}/\text{NF}$  ( $-0.091$ ,  $-0.285$ , and  $-0.381 \text{ V}$ ),  $\text{Ni}_2\text{P}-\text{NiSe}_2/\text{MoO}_x/\text{NF}$  only requires the lower potentials of  $-0.082$ ,  $-0.227$ , and  $-0.271 \text{ V}$  to afford the cathodic current densities of  $100$ ,  $500$ , and  $1000 \text{ mA cm}^{-2}$  (Fig. 4d). Such activity performance verifies the significant potential and high efficiency of  $\text{Ni}_2\text{P}-\text{NiSe}_2/\text{MoO}_x/\text{NF}$  for practical applications.

In addition to its excellent HER activity, long-term stability is

another crucial parameter for practical applications. Remarkably, as confirmed by a chronoamperometry test at a potential of  $-0.20 \text{ V}$  vs. RHE (Fig. 4e),  $\text{Ni}_2\text{P}-\text{NiSe}_2/\text{MoO}_x/\text{NF}$  exhibits superior stability over  $200 \text{ h}$ , consistently delivering a larger current density of approximately  $-330 \text{ mA cm}^{-2}$ . In contrast, the noble-metal  $\text{Pt}/\text{C}/\text{NF}$  catalyst shows a noticeable decrease in current under identical conditions. After stability test, further characterizations including XRD, SEM, TEM (Fig. S23), and XPS (Fig. S24) demonstrate that the crystal structure, morphology, composition, and surface valence states of  $\text{Ni}_2\text{P}-\text{NiSe}_2/\text{MoO}_x/\text{NF}$  are largely preserved, verifying the outstanding structural robustness.

The electrochemical performance of catalysts is strongly influenced by their mass transport capacity, which can be evaluated by their wettability [43]. To quantitatively analyze the wettability differences among various catalysts, the contact angle (CA) measurements are conducted. Fig. 4f reveals that  $\text{Ni}_2\text{P}-\text{NiSe}_2/\text{MoO}_x/\text{NF}$  exhibits the smallest water contact angle (CA) at  $3.2^\circ$ , in contrast to  $\text{Pt}/\text{C}/\text{NF}$  ( $115.8^\circ$ ) and bare NF ( $123.9^\circ$ ), which implies the remarkable hydrophilicity of  $\text{Ni}_2\text{P}-\text{NiSe}_2/\text{MoO}_x/\text{NF}$ . Furthermore, the bubble CAs (Fig. 4g) of  $\text{Ni}_2\text{P}-\text{NiSe}_2/\text{MoO}_x/\text{NF}$  ( $159.8^\circ$ ) is larger than  $\text{Pt}/\text{C}/\text{NF}$  ( $146.5^\circ$ ), and bare NF ( $136.2^\circ$ ), indicating the superior aerophobicity of  $\text{Ni}_2\text{P}-\text{NiSe}_2/\text{MoO}_x/\text{NF}$ . These combined results demonstrate efficient mass transfer and the release of gas bubbles on the surface of  $\text{Ni}_2\text{P}-\text{NiSe}_2/\text{MoO}_x/\text{NF}$ . As shown in Fig. 4h, gas bubbles firmly adhere to the surface of bare NF and  $\text{Pt}/\text{C}/\text{NF}$ , rapidly growing to large sizes ranging from  $300$  to  $800 \mu\text{m}$ . In contrast, for  $\text{Ni}_2\text{P}-\text{NiSe}_2/\text{MoO}_x/\text{NF}$ , small size of bubbles ( $\leq 300 \mu\text{m}$ ) are able to easily escape from the surface into the solution. According to the solid-liquid-gas interface theory, rough electrode surfaces favor the formation of discontinuous contact three-phase interfaces, resulting in a notably reduced contact region between bubbles and electrode surfaces, thus facilitating the adsorption and desorption of reactants and gaseous products [44].

In summary, all the electrochemical measurements presented in this study unequivocally demonstrate the exceptional activity and stability of  $\text{Ni}_2\text{P}-\text{NiSe}_2/\text{MoO}_x$  heterostructures toward alkaline HER. This remarkable performance can be attributed to the collaborative effects of the coupling interface and array structure, which optimize local charge distribution and mass transfer. As a result, these heterostructures contribute to highly efficient water electrolysis performance even under higher current densities. Furthermore, to meet the requirements of large-scale applications, a larger-sized  $\text{Ni}_2\text{P}-\text{NiSe}_2/\text{MoO}_x/\text{NF}$  electrode with an area of  $4 \times 10 \text{ cm}^2$  is prepared and tested for alkaline HER. The corresponding structural characterization (Fig. S25) and electrochemical tests (Fig. S26) exhibit the identical nanorod morphology and excellent HER activity of the fabricated heterostructure catalysts, which proves the significant potential of this synthetic strategy to large-scale prepare highly-efficient HER electrocatalysts.

To fully utilize the as-fabricated heterostructure catalysts, we further investigate OER activity of  $\text{Ni}_2\text{P}-\text{NiSe}_2/\text{MoO}_x/\text{NF}$  in  $\text{O}_2$ -saturated  $1.0 \text{ M KOH}$ , using precious  $\text{RuO}_2/\text{NF}$  as a benchmark catalyst.  $iR$ -compensated cyclic voltammetry (CV) curves are displayed in Fig. S27a. Impressively,  $\text{Ni}_2\text{P}-\text{NiSe}_2/\text{MoO}_x/\text{NF}$  exhibits extraordinary activity, requiring overpotentials of  $241$  and  $592 \text{ mV}$  to achieve current densities of  $10$  and  $500 \text{ mA cm}^{-2}$ , respectively (determined from cathodic sweep curves to avoid interface catalyst oxidation features, Fig. S27b). These values are significantly superior to those of  $\text{RuO}_2/\text{NF}$  and other fabricated catalysts (Fig. S27c), as well as many reported OER catalysts (Table S2). When the testing conditions are changed to  $30\%$  KOH at  $85^\circ\text{C}$ , the anodic potentials required to achieve  $500$  and  $1000 \text{ mA cm}^{-2}$  are only  $351$  and  $403 \text{ mV}$ , respectively (Fig. S28), indicating the accelerated reaction kinetics. Determined from their Tafel plots (Fig. S29a,b),  $\text{Ni}_2\text{P}-\text{NiSe}_2/\text{MoO}_x/\text{NF}$  exhibits the lowest Tafel slope of  $34.9 \text{ mV dec}^{-1}$  compared to other samples, indicating excellent kinetic performance. The smallest  $R_{ct}$  value of  $\text{Ni}_2\text{P}-\text{NiSe}_2/\text{MoO}_x/\text{NF}$  (Fig. S29c,d) demonstrates that multiple heterostructures synergistically promotes charge transfer kinetics at the electrode-electrolyte interface during OER. Multiple-step chronoamperometry measurements (Fig. S30) of  $\text{Ni}_2\text{P}-\text{NiSe}_2/\text{MoO}_x/\text{NF}$

demonstrate great durability over 130 h with negligible fluctuations under current densities ranging from approximately 100 to 360  $\text{mA cm}^{-2}$ . After the OER stability test, XPS results (Fig. S31) reveals that P and Se nearly disappeared, while the surface oxygen and metal-oxygen bonding increase significantly. This is further evidenced by EDX mapping results (Fig. S32), collectively indicating the phase transformation of  $\text{Ni}_2\text{P}-\text{NiSe}_2/\text{MoO}_x$  to nickel hydr(oxy)oxides [45]. Meantime, the nanorod arrays are still preserved (Fig. S33), although the surface of the nanorods became rough, and some nanosheets coat the surface of the nanorods. In situ transformed nickel hydr(oxy)oxides from the initial oxidation of  $\text{Ni}_2\text{P}-\text{NiSe}_2/\text{MoO}_x/\text{NF}$  during the OER process could serve as the real active species for alkaline OER, similar to the reported precedents, thereby leading to the excellent OER activity and stability [46]. Subsequently, the adsorption free energy of oxygen intermediates are calculated based on different models to investigate the relationship between electronic structure and OER performance on the reconstructed structures. The primitive steps of OER process on the optimized models, including  $^*\text{OH}$ ,  $^*\text{O}$ , and  $^*\text{OOH}$  intermediates, are outlined in Fig. S34. Compared with  $\text{Ni}(\text{OH})_2$  and  $\text{Ni}_2\text{P}-\text{NiSe}_2/\text{MoO}_2$ , the energy barrier of the rate-determining step (RDS) involving deprotonation from  $^*\text{OH}$  to  $^*\text{O}$  for  $\text{Ni}(\text{OH})_2/\text{MoO}_2$  is significantly reduced to

1.12 eV, suggesting the formation of nickel hydr(oxy)oxides species and the heterostructures are more thermodynamically favorable for catalyzing the OER.

### 3.4. Overall water splitting performance

Inspired by the excellent performance of  $\text{Ni}_2\text{P}-\text{NiSe}_2/\text{MoO}_x/\text{NF}$  in both HER and OER in alkaline media, a full water-splitting electrolyzer is assembled using  $\text{Ni}_2\text{P}-\text{NiSe}_2/\text{MoO}_x/\text{NF}$  as bifunctional electrodes in a 1.0 M KOH electrolyte. A noble-metal couple consisting of  $\text{RuO}_2/\text{NF}(+)$  as the anode and  $\text{Pt/C}/\text{NF}(-)$  as the cathode is also investigated for comparison. As shown in Fig. 5a, the overall water-splitting polarization curve of  $\text{Ni}_2\text{P}-\text{NiSe}_2/\text{MoO}_x/\text{NF}$  exhibits extremely low cell voltages of 1.63, 1.76, and 1.90 V at 50, 100, and 200  $\text{mA cm}^{-2}$ , respectively, which outperform the  $\text{RuO}_2/\text{NF} = |\text{Pt/C}/\text{NF}$  (1.73, 1.90, and 2.14 V) and  $\text{Ni}_2\text{P}-\text{NiSe}_2/\text{NF}$  (1.83, 1.95 and 2.15 V). Furthermore, the optical photograph in Fig. 5b demonstrates that a single commercial battery with a working voltage of 1.5 V could drive the water-splitting electrolyzer with observable gas production, confirming the excellent electric energy-to-hydrogen conversion rate. Remarkably, the required voltage of  $\text{Ni}_2\text{P}-\text{NiSe}_2/\text{MoO}_x/\text{NF}$  to achieve a current density of

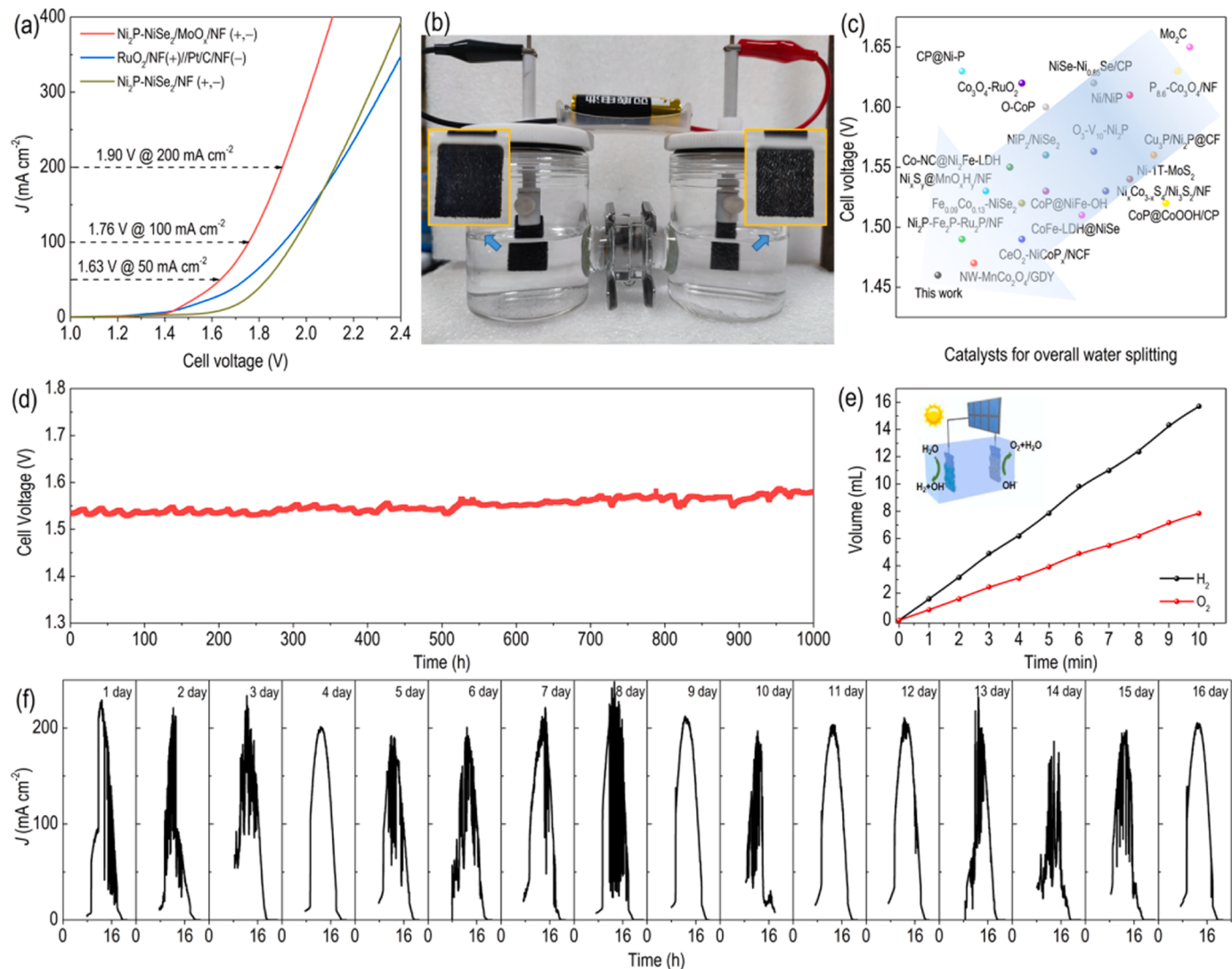


**Fig. 5.** (a) LSV polarization curves of overall water splitting in 1.0 KOH + 25 °C. (b) Photo showing single-battery-powered overall water splitting. (c) Comparison of the required voltage to afford the current density of 10  $\text{mA cm}^{-2}$  for  $\text{Ni}_2\text{P}-\text{NiSe}_2/\text{MoO}_x/\text{NF}$  in this work with other bifunctional catalysts. (d) Chronopotentiometric curve of  $\text{Ni}_2\text{P}-\text{NiSe}_2/\text{MoO}_x/\text{NF}$  at 20  $\text{mA cm}^{-2}$  for overall water splitting. (e) Experimental volumes of  $\text{H}_2$  and  $\text{O}_2$  by the  $\text{Ni}_2\text{P}-\text{NiSe}_2/\text{MoO}_x/\text{NF}$  electrode varying with time in a sealed H-type electrolyzer derived by solar energy. (f) Current density versus time curves of water electrolyzer powered by solar energy.

10 mA cm<sup>-2</sup> also surpasses most of the Co- or Ni-containing bifunctional catalysts for alkaline overall water splitting (Fig. 5c). Through measurement of the generated H<sub>2</sub> and O<sub>2</sub> via the water displacement method (Fig. S35), it is determined that the produced H<sub>2</sub> on the cathode and O<sub>2</sub> on the anode in this Ni<sub>2</sub>P-NiSe<sub>2</sub>/MoO<sub>x</sub>/NF-catalyzed electrolyzer exhibits a stoichiometry of 2:1 within 120 min of continuous operation, indicating nearly 100% Faradaic efficiency. What's more, according to the steady-state electrochemical analysis at a current density of 20 mA cm<sup>-2</sup> shown in Fig. 5d, Ni<sub>2</sub>P-NiSe<sub>2</sub>/MoO<sub>x</sub>/NF maintains its extraordinary activity for more than 1000 h, meeting the stringent criteria for commercial utilization. Finally, when combined with the results of SEM (Fig. S36) and XRD (Fig. S37) after the durability test, it can be concluded that the structure of Ni<sub>2</sub>P-NiSe<sub>2</sub>/MoO<sub>x</sub>/NF is largely retained. Notably, the overall water splitting activity and stability of Ni<sub>2</sub>P-NiSe<sub>2</sub>/MoO<sub>x</sub>/NF ranks among the top values of non-noble metal-based catalysts reported recently (Table S3).

The feasibility of producing green hydrogen without carbon emission using renewable electricity is further demonstrated by integrating the water electrolyzer with a commercially available silicon solar cell (Fig. S38a,b). With solar-driven electricity as the power source, the bifunctional Ni<sub>2</sub>P-NiSe<sub>2</sub>/MoO<sub>x</sub>/NF electrode rapidly catalyzes water

splitting with continuous release of gas bubbles. In just 10 min, a volume of 15.7 mL of H<sub>2</sub> is obtained (Fig. 5e, Fig. S38c), corresponding to an impressive H<sub>2</sub> production rate of 26.17  $\mu\text{L s}^{-1}$ , demonstrating the promising potential for practical utilization. To evaluate the performance of the integrated system in an outdoor environment, chronoamperometry curves of the water-splitting unit powered by solar energy are conducted under natural lighting conditions. As shown in Fig. 5f, the measured current density exhibits synchronous fluctuations associated with variations in light intensity, with the highest current densities consistently obtained at midday. Fluctuations in current, as observed in Fig. 5f, are common challenges encountered in renewable energy-powered electrolyzers [47]. Furthermore, this integrated hydrogen production unit maintains stable operation over 16 days. These exciting results indicate the exceptional catalytic activity and durability of Ni<sub>2</sub>P-NiSe<sub>2</sub>/MoO<sub>x</sub>/NF for alkaline water electrolysis, making it a promising candidate for sustainable green hydrogen production.

In industrial water electrolysis system, the operating temperature typically ranges from about 50 to 90 °C, aiming to reduce the overall voltage required for water splitting further [48]. The electrochemical performance of water-splitting electrolyzer can be evaluated at

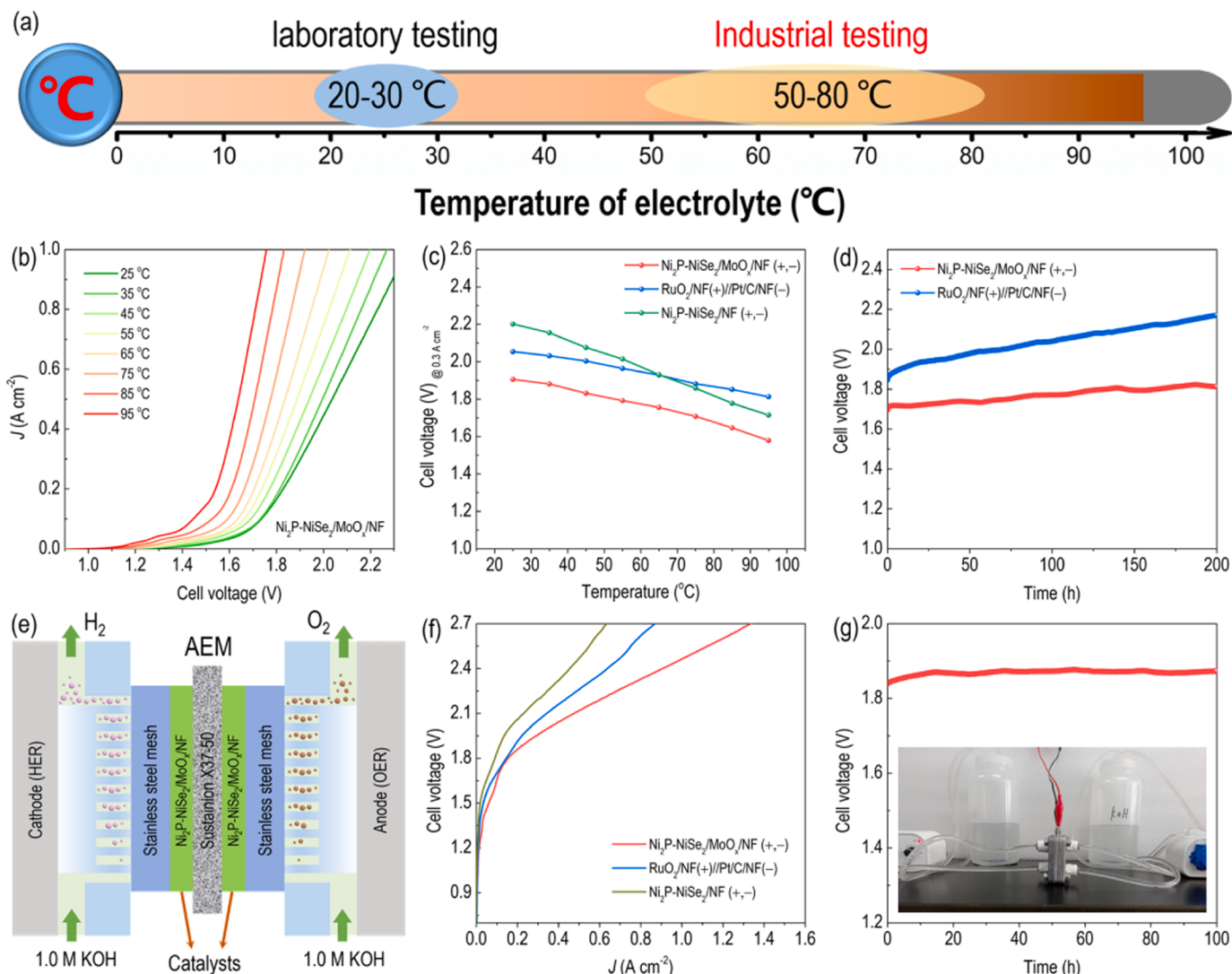


Fig. 6. (a) The temperature difference between laboratory testing and industrial testing. (b) Polarization curves of Ni<sub>2</sub>P-NiSe<sub>2</sub>/MoO<sub>x</sub>/NF for overall water splitting at different temperatures in 30% KOH electrolyte. (c) Overall water splitting voltages at 300 mA cm<sup>-2</sup> under various temperatures. (d) Chronopotentiometric curves at 200 mA cm<sup>-2</sup> under 30% KOH + 65 °C. (e) Schematic illustration of an alkaline AEM cell. (f) Polarization curves for water electrolysis. (g) Chronopotentiometric curve at 200 mA cm<sup>-2</sup> and the photograph of AEM cell.

industrial temperatures (50–90 °C) to bridge the gap between laboratory testing and industrial application (Fig. 6a). Overall water splitting polarization curves of  $\text{Ni}_2\text{P}-\text{NiSe}_2/\text{MoO}_x/\text{NF}$  are measured over a range of temperatures. In Fig. 6b, as the temperature of the alkaline electrolyte gradually increases, the voltage required by  $\text{Ni}_2\text{P}-\text{NiSe}_2/\text{MoO}_x/\text{NF}$  electrode to split water decreases at the same current density. When the current density is set at 300  $\text{mA cm}^{-2}$  (Fig. 6c), the water-splitting voltages of  $\text{Ni}_2\text{P}-\text{NiSe}_2/\text{MoO}_x/\text{NF}$  are consistently lower than those of  $\text{RuO}_2/\text{NF}(+)||\text{Pt/C/NF}(-)$  and  $\text{Ni}_2\text{P}-\text{NiSe}_2/\text{NF}$  at different temperatures. The electrochemical stability evaluation of  $\text{Ni}_2\text{P}-\text{NiSe}_2/\text{MoO}_x/\text{NF}$  is conducted at 200  $\text{mA cm}^{-2}$  and 65 °C. As shown in Fig. 6d, the overall water-splitting voltages of  $\text{Ni}_2\text{P}-\text{NiSe}_2/\text{MoO}_x/\text{NF}$  decay at a slower rate (0.58  $\text{mV h}^{-1}$ ) compared to  $\text{RuO}_2/\text{NF}(+)||\text{Pt/C/NF}(-)$  (1.5  $\text{mV h}^{-1}$ ). This suggests the superior operational durability of  $\text{Ni}_2\text{P}-\text{NiSe}_2/\text{MoO}_x/\text{NF}$  at elevated temperatures and high current densities, further highlighting its potential for industrial applications.

In addition to the above assessments, an alkaline anion exchange membrane (AEM) cell was constructed to evaluate the potential application of  $\text{Ni}_2\text{P}-\text{NiSe}_2/\text{MoO}_x/\text{NF}$  in industrial conditions. The structure of the assembled AEM water electrolyzer is detailed in Fig. 6e. An AEM cell utilizing  $\text{Ni}_2\text{P}-\text{NiSe}_2/\text{MoO}_x/\text{NF}$  as the catalyst exhibits lower overpotentials compared to  $\text{RuO}_2/\text{NF}(+)||\text{Pt/C/NF}(-)$  and  $\text{Ni}_2\text{P}-\text{NiSe}_2/\text{NF}$  across a range of current densities (Fig. 6f), as well as in the transitional alkaline water electrolysis (AWE). This improved performance in the AEM cell is attributed to the reduced charge transfer resistance in AEM compared to AWE. Furthermore, the assembled AEM cell demonstrates remarkable stability for 100 h at 200  $\text{mA cm}^{-2}$  (Fig. 6g). Based on these results,  $\text{Ni}_2\text{P}-\text{NiSe}_2/\text{MoO}_x/\text{NF}$  is considered as a promising candidate for large-scale hydrogen production in industrial applications.

The exceptional catalytic performance exhibited by  $\text{Ni}_2\text{P}-\text{NiSe}_2/\text{MoO}_x/\text{NF}$  catalyst can be ascribed to several key factors: (i) The intricate synergy and cooperative interactions among multiple interfaces play a pivotal role in the modification of the electronic structure, leading to an optimized adsorption capacity for reaction intermediates. (ii) The resulting electrode comprising  $\text{Ni}_2\text{P}-\text{NiSe}_2/\text{MoO}_x/\text{NF}$  heterostructures significantly facilitates interfacial electron transport between these heterostructures and the underlying nickel foam substrate. This enhancement in interfacial electron transport is instrumental in bolstering both mass activity and intrinsic activity of the active species. (iii) The robust catalyst-substrate interaction and a reduced metal dissolution rate contribute prominently to the heightened stability exhibited by  $\text{Ni}_2\text{P}-\text{NiSe}_2/\text{MoO}_x/\text{NF}$ , ensuring its sustained catalytic performance over extended operational periods. (iv) The strategic nanengineering of  $\text{Ni}_2\text{P}-\text{NiSe}_2/\text{MoO}_x/\text{NF}$  nanorod arrays serves as an effective mitigation strategy to mitigate the adverse effects associated with gas bubble adhesion during the electrocatalytic process.

#### 4. Conclusions

In summary, this study introduces a facile and scalable strategy for the synthesis of heterointerface-rich  $\text{Ni}_2\text{P}-\text{NiSe}_2/\text{MoO}_x$  nanorods, designed for highly efficient HER under larger current densities. As expected, the synergistic coupling interactions among  $\text{Ni}_2\text{P}$ ,  $\text{NiSe}_2$ , and  $\text{MoO}_x$  within the heterostructures serve to finely modulate charge density and electronic structure, thereby expediting the kinetics of critical initial steps in alkaline HER. The resulting  $\text{Ni}_2\text{P}-\text{NiSe}_2/\text{MoO}_x/\text{NF}$  exhibits remarkably low overpotentials and exceptional stability during laboratory testing (1.0 M KOH + 25 °C) as well as under industrial conditions (30% KOH + 65 °C). These findings effectively bridge the gap between laboratory-scale and industrial-scale water electrolysis applications. Furthermore, encouraged by the outstanding alkaline oxygen evolution performance of  $\text{Ni}_2\text{P}-\text{NiSe}_2/\text{MoO}_x/\text{NF}$ , the assembly of a full water electrolyzer demonstrates exceptional overall water-splitting performance and robust stability, even under elevated current densities within industrial settings. Moreover, when employed in the AEM water electrolyzer, this  $\text{Ni}_2\text{P}-\text{NiSe}_2/\text{MoO}_x/\text{NF}$  catalyst still exhibits

consistently impressive performance, underscoring its immense potential for large-scale hydrogen production. This work represents a systematic and rational approach to harness heterostructure engineering in the construction of complementary materials, thereby accelerating the development of active catalysts for electrocatalytic processes and beyond.

#### CRediT authorship contribution statement

**Wang Hao-Yu:** Investigation. **Tian Wen-Wen:** Investigation. **Zhai Si-Xiang:** Investigation. **Feng Yi:** Investigation. **Yuan Zhong-Yong:** Writing – review & editing, Supervision, Project administration, Funding acquisition. **Ren Jin-Tao:** Writing – review & editing, Writing – original draft, Methodology, Investigation, Funding acquisition, Conceptualization. **Chen Lei:** Investigation.

#### Declaration of Competing Interest

The authors declare that they have no known competing financial interests or personal relationships that could have appeared to influence the work reported in this paper.

#### Data Availability

Data will be made available on request.

#### Acknowledgments

This work was supported by the National Natural Science Foundation of China (22105108, and 22179065), and China Postdoctoral Science Foundation (2020M680860).

#### Appendix A. Supporting information

Supplementary data associated with this article can be found in the online version at [doi:10.1016/j.apcatb.2024.123817](https://doi.org/10.1016/j.apcatb.2024.123817).

#### References

- [1] Z.Y. Yu, Y. Duan, X.Y. Feng, X. Yu, M.R. Gao, S.H. Yu, Clean and and affordable hydrogen fuel from alkaline water splitting: past, recent progress, and future prospects, *Adv. Mater.* 33 (2021) 2007100, <https://doi.org/10.1002/adma.202007100>.
- [2] C. Hu, L. Zhang, J. Gong, Recent progress made in the mechanism comprehension and design of electrocatalysts for alkaline water splitting, *Energy Environ. Sci.* 12 (2019) 2620–2645, <https://doi.org/10.1039/c9ee01202h>.
- [3] A. Kumar, V.Q. Bui, J. Lee, A.R. Jadhav, Y. Hwang, M.G. Kim, Y. Kawazoe, H. Lee, Modulating interfacial charge density of  $\text{NiP}_2-\text{FeP}_2$  via coupling with metallic Cu for accelerating alkaline hydrogen evolution, *ACS Energy Lett.* 6 (2021) 354–363, <https://doi.org/10.1021/acsenergylett.0c02498>.
- [4] Y. Li, S. Guo, T. Jin, Y. Wang, F. Cheng, L. Jiao, Promoted synergy in core-branch  $\text{CoP}@\text{NiFe-OH}$  nanohybrids for efficient electrochemical-/photovoltage-driven overall water splitting, *Nano Energy* 63 (2019) 103821, <https://doi.org/10.1016/j.nanoen.2019.06.017>.
- [5] S. Jiao, X. Fu, S. Wang, Y. Zhao, Perfecting electrocatalysts via imperfections: towards the large-scale deployment of water electrolysis technology, *Energy Environ. Sci.* 14 (2021) 1722–1770, <https://doi.org/10.1039/d0ee03635h>.
- [6] H. Sun, X. Xu, Y. Song, W. Zhou, Z. Shao, Designing high-valence metal sites for electrochemical water splitting, *Adv. Funct. Mater.* 31 (2021) 2009779, <https://doi.org/10.1002/adfm.202009779>.
- [7] W.J. Jiang, T. Tang, Y. Zhang, J.S. Hu, Synergistic modulation of non-precious-metal electrocatalysts for advanced water splitting, *Acc. Chem. Res.* 53 (2020) 1111–1123, <https://doi.org/10.1021/acs.accounts.0c00127>.
- [8] J.T. Ren, L. Chen, H.Y. Wang, W.W. Tian, Z.Y. Yuan, Water electrolysis for hydrogen production: from hybrid systems to self-powered/catalyzed devices, *Energy Environ. Sci.* 17 (2024) 49–113, <https://doi.org/10.1039/D3EE02467A>.
- [9] F. Zhang, X. Wang, W. Han, Y. Qian, L. Qiu, Y. He, L. Lei, X. Zhang, The synergistic activation of Ce-doping and  $\text{CoP}/\text{Ni}_3\text{P}$  hybrid interaction for efficient water splitting at large-current-density, *Adv. Funct. Mater.* 33 (2022) 2212381, <https://doi.org/10.1002/adfm.202212381>.
- [10] X. Zhou, Y. Mo, F. Yu, L. Liao, X. Yong, F. Zhang, D. Li, Q. Zhou, T. Sheng, H. Zhou, Engineering active iron sites on nanoporous bimetal phosphide/nitride heterostructure array enabling robust overall water splitting, *Adv. Funct. Mater.* 33 (2022) 2209465, <https://doi.org/10.1002/adfm.202209465>.

[11] D. Chen, H. Bai, J. Zhu, C. Wu, H. Zhao, D. Wu, J. Jiao, P. Ji, S. Mu, Multiscale hierarchical structured NiCoP enabling ampere-level water splitting for multi-scenarios green energy-to-hydrogen systems, *Adv. Energy Mater.* 13 (2023) 2300499, <https://doi.org/10.1002/aenm.202300499>.

[12] Y. Du, B. Li, G. Xu, L. Wang, Recent advances in interface engineering strategy for highly-efficient electrocatalytic water splitting, *InfoMat* 5 (2022) e12377, <https://doi.org/10.1002/inf2.12377>.

[13] H. Lei, Q. Wan, S. Tan, Z. Wang, W. Mai, Pt-quantum-dot-modified sulfur-doped NiFe layered double hydroxide for high-current-density alkaline water splitting at industrial temperature, *Adv. Mater.* 35 (2023) 2208209, <https://doi.org/10.1002/adma.202208209>.

[14] H. Ma, Z. Chen, Z. Wang, C.V. Singh, Q. Jiang, Interface engineering of Co/CoMoN/NF heterostructures for high-performance electrochemical overall water splitting, *Adv. Sci.* 9 (2022) 2105313, <https://doi.org/10.1002/advs.202105313>.

[15] C. Pei, M.C. Kim, Y. Li, C. Xia, J. Kim, W. So, X. Yu, H.S. Park, J.K. Kim, Electron transfer-induced metal spin-crossover at NiCo<sub>2</sub>S<sub>4</sub>/ReS<sub>2</sub> 2D–2D interfaces for promoting pH-universal hydrogen evolution reaction, *Adv. Funct. Mater.* 33 (2022) 2210072, <https://doi.org/10.1002/adfm.202210072>.

[16] H. Yu, S. Zhu, Y. Hao, Y.M. Chang, L. Li, J. Ma, H.Y. Chen, M. Shao, S. Peng, Modulating local interfacial bonding environment of heterostructures for energy-saving hydrogen production at high current densities, *Adv. Funct. Mater.* 33 (2023) 2212811, <https://doi.org/10.1002/adfm.202212811>.

[17] X. Xiao, L. Yang, W. Sun, Y. Chen, H. Yu, K. Li, B. Jia, L. Zhang, T. Ma, Electrocatalytic water splitting: from harsh and mild conditions to natural seawater, *Small* 18 (2022) 2105830, <https://doi.org/10.1002/smll.202105830>.

[18] Q. Wen, Y. Zhao, Y. Liu, H. Li, T. Zhai, Ultrahigh-current-density and long-term-durability electrocatalysts for water splitting, *Small* 18 (2022) 2104513, <https://doi.org/10.1002/smll.202104513>.

[19] H. Sun, X. Xu, H. Kim, W. Jung, W. Zhou, Z. Shao, Electrochemical water splitting: bridging the gaps between fundamental research and industrial applications, *Energy Environ. Mater.* 6 (2023) e12441, <https://doi.org/10.1002/eem2.12441>.

[20] J. Liu, X. Yang, F. Si, B. Zhao, X. Xi, L. Wang, J. Zhang, X.Z. Fu, J.L. Luo, Interfacial component coupling effects towards precise heterostructure design for efficient electrocatalytic water splitting, *Nano Energy* 103 (2022) 107753, <https://doi.org/10.1016/j.nanoen.2022.107753>.

[21] H. Yang, M. Driess, P.W. Menezes, Self-Supported electrocatalysts for practical water electrolysis, *Adv. Energy Mater.* 11 (2021) 2102074, <https://doi.org/10.1002/aenm.202102074>.

[22] P. Wang, Z. Pu, W. Li, J. Zhu, C. Zhang, Y. Zhao, S. Mu, Coupling NiSe<sub>2</sub>-Ni<sub>2</sub>P heterostructure nanowrinkles for highly efficient overall water splitting, *J. Catal.* 377 (2019) 600–608, <https://doi.org/10.1016/j.jcat.2019.08.005>.

[23] Y. An, X. Long, M. Ma, J. Hu, H. Lin, D. Zhou, Z. Xing, B. Huang, S. Yang, One-step controllable synthesis of catalytic Ni<sub>4</sub>Mo/MoO<sub>x</sub>/Cu nanointerfaces for highly efficient water reduction, *Adv. Energy Mater.* 9 (2019) 1901454, <https://doi.org/10.1002/aenm.201901454>.

[24] C. Liu, T. Gong, J. Zhang, X. Zheng, J. Mao, H. Liu, Y. Li, Q. Hao, Engineering Ni<sub>2</sub>P-NiSe<sub>2</sub> heterostructure interface for highly efficient alkaline hydrogen evolution, *Appl. Catal. B* 262 (2020) 118245, <https://doi.org/10.1016/j.apcatb.2019.118245>.

[25] J.T. Ren, L. Chen, H.Y. Wang, W.W. Tian, X.L. Song, Q.H. Kong, Z.Y. Yuan, Synergistic activation of crystalline Ni<sub>2</sub>P and amorphous NiMoO<sub>x</sub> for efficient water splitting at high current densities, *ACS Catal.* 13 (2023) 9792–9805, <https://doi.org/10.1021/acscatal.3c01885>.

[26] G. Qian, J. Chen, T. Yu, J. Liu, L. Luo, S. Yin, Three-phase heterojunction nimo-based nano-needle for water splitting at industrial alkaline condition, *Nano-Micro Lett.* 14 (2021) 20, <https://doi.org/10.1007/s40820-021-00744-x>.

[27] Q. Zhang, Y. Deng, Z. Hu, Y. Liu, M. Yao, P. Liu, Searchin-like hierarchical NiCo<sub>2</sub>O<sub>4</sub>/NiMoO<sub>4</sub> core-shell nanomaterials for high performance supercapacitors, *Phys. Chem. Chem. Phys.* 16 (2014) 23451–23460, <https://doi.org/10.1039/c4cp02928c>.

[28] X. Li, W.Q. Huang, L.X. Xia, Y.Y. Li, H.W. Zhang, S.F. Ma, Y.M. Wang, X.J. Wang, G. F. Huang, NiFe<sub>2</sub>O<sub>4</sub>/NiFeP heterostructure grown on nickel foam as an efficient electrocatalyst for water oxidation, *ChemElectroChem* 7 (2020) 4047–4054, <https://doi.org/10.1002/celc.202000958>.

[29] Z.Y. Yu, C.C. Lang, M.-R. Gao, Y. Chen, Q.Q. Fu, Y. Duan, S.H. Yu, Ni-Mo-O nanorod-derived composite catalysts for efficient alkaline water-to-hydrogen conversion via urea electrolysis, *Energy Environ. Sci.* 11 (2018) 1890–1897, <https://doi.org/10.1039/c8ee00521d>.

[30] X. Zhang, S. Zhang, J. Li, E. Wang, One-step synthesis of well-structured Ni<sub>3</sub>Ni<sub>2</sub>P<sub>2</sub>S<sub>6</sub> nanosheets on nickel foam for efficient overall water splitting, *J. Mater. Chem. A* 5 (2017) 22131–22136, <https://doi.org/10.1039/c7ta05285e>.

[31] W. Jiang, J. Sun, K. Lu, C. Jiang, H. Xu, Z. Huang, N. Cao, F. Dai, 2D coordination polymer-derived CoSe<sub>2</sub>-NiSe<sub>2</sub>/CN nanosheets: the dual-phase synergistic effect and ultrathin structure to enhance the hydrogen evolution reaction, *Dalton Trans.* 50 (2021) 9934–9941, <https://doi.org/10.1039/d1dt01487k>.

[32] Y. Li, X. Yu, J. Gao, Y. Ma, Structural and electronic modulation of (Fe,Ni)P@Ni<sub>2</sub>P heterostructure for efficient overall water splitting at high current density, *Chem. Eng. J.* 470 (2023) 144373, <https://doi.org/10.1016/j.cej.2023.144373>.

[33] Y. Zhao, N. Dongfang, C.A. Triana, C. Huang, R. Erni, W. Wan, J. Li, D. Stoian, L. Pan, P. Zhang, J. Lan, M. Iannuzzi, G.R. Patzke, Dynamics and control of active sites in hierarchically nanostructured cobalt phosphide/chalcogenide-based electrocatalysts for water splitting, *Energy Environ. Sci.* 15 (2022) 727–739, <https://doi.org/10.1039/d1ee02249k>.

[34] T. Li, Q. Zhang, X.H. Wang, J. Luo, L. Shen, H.C. Fu, F. Gu, N.B. Li, H.Q. Luo, Selenium-induced NiSe<sub>2</sub>@CuSe<sub>2</sub> hierarchical heterostructure for efficient oxygen evolution reaction, *Nanoscale* 13 (2021) 17846–17853, <https://doi.org/10.1039/d1nr05109a>.

[35] X. Wu, J. Li, Y. Li, Z. Wen, NiFeP-MoO<sub>2</sub> hybrid nanorods on nickel foam as high-activity and high-stability electrode for overall water splitting, *Chem. Eng. J.* 409 (2021) 128161, <https://doi.org/10.1016/j.cej.2020.128161>.

[36] J.T. Ren, L. Wang, L. Chen, X.L. Song, Q.H. Kong, H.Y. Wang, Z.Y. Yuan, Interface metal oxides regulating electronic state around nickel species for efficient alkaline hydrogen electrocatalysis, *Small* 19 (2023) 2206196, <https://doi.org/10.1002/smll.202206196>.

[37] W. Zhang, Y. Zou, H. Liu, S. Chen, X. Wang, H. Zhang, X. She, D. Yang, Single-crystalline (Fe<sub>x</sub>Ni<sub>1-x</sub>)<sub>2</sub>P nanosheets with dominant {0111} facets: Efficient electrocatalysts for hydrogen evolution reaction at all pH values, *Nano Energy* 56 (2019) 813–822, <https://doi.org/10.1016/j.nanoen.2018.11.090>.

[38] L. Yang, L. Huang, Y. Yao, L. Jiao, In-situ construction of lattice-matching NiP<sub>2</sub>/NiSe<sub>2</sub> heterointerfaces with electron redistribution for boosting overall water splitting, *Appl. Catal. B* 282 (2021) 119584, <https://doi.org/10.1016/j.apcatb.2020.119584>.

[39] G. Yang, Y. Jiao, H. Yan, Y. Xie, A. Wu, X. Dong, D. Guo, C. Tian, H. Fu, Interfacial engineering of MoO<sub>2</sub>-FeP heterojunction for highly efficient hydrogen evolution coupled with biomass electrooxidation, *Adv. Mater.* 32 (2020) 2000455, <https://doi.org/10.1002/adma.202000455>.

[40] Q. Zhang, X. Li, W. Yi, W. Li, H. Bai, J. Liu, G. Xi, Plasmonic MoO<sub>2</sub> nanospheres as a highly sensitive and stable non-noble metal substrate for multicomponent surface-enhanced raman analysis, *Anal. Chem.* 89 (2017) 11765–11771, <https://doi.org/10.1021/acs.analchem.7b03385>.

[41] L. Yuan, S. Liu, S. Xu, X. Yang, J. Bian, C. Lv, Z. Yu, T. He, Z. Huang, D. W. Boukhvalov, C. Cheng, Y. Huang, C. Zhang, Modulation of Volmer step for efficient alkaline water splitting implemented by titanium oxide promoting surface reconstruction of cobalt carbonate hydroxide, *Nano Energy* 82 (2021) 105732, <https://doi.org/10.1016/j.nanoen.2020.105732>.

[42] Y. Xie, Y. Sun, H. Tao, X. Wang, J. Wu, K. Ma, L. Wang, Z. Kang, Y. Zhang, In situ investigation on life-time dynamic structure–performance correlation toward electrocatalyst service behavior in water splitting, *Adv. Funct. Mater.* 32 (2022) 211177, <https://doi.org/10.1002/adfm.202111777>.

[43] J. Hou, Y. Wu, B. Zhang, S. Cao, Z. Li, L. Sun, Rational design of nanoarray architectures for electrocatalytic water splitting, *Adv. Funct. Mater.* 29 (2019) 1808367, <https://doi.org/10.1002/adfm.201808367>.

[44] X. Shan, J. Liu, H. Mu, Y. Xiao, B. Mei, W. Liu, G. Lin, Z. Jiang, L. Wen, L. Jiang, An engineered superhydrophilic/superaerophobic electrocatalyst composed of the supported CoMoS<sub>x</sub> chalcogel for overall water splitting, *Angew. Chem. Int. Ed.* 59 (2020) 1659–1665, <https://doi.org/10.1002/anie.201911617>.

[45] Y. Zeng, M. Zhao, Z. Huang, W. Zhu, J. Zheng, Q. Jiang, Z. Wang, H. Liang, Surface reconstruction of water splitting electrocatalysts, *Adv. Energy Mater.* 12 (2022) 2201713, <https://doi.org/10.1002/aenm.202201713>.

[46] X. Luo, X. Tan, P. Ji, L. Chen, J. Yu, S. Mu, Surface reconstruction-derived heterostructures for electrochemical water splitting, *EnergyChem* 5 (2023) 100091, <https://doi.org/10.1016/j.enchem.2022.100091>.

[47] M. Chatenet, B.G. Pollet, D.R. Dekel, F. Dionigi, J. Deseure, P. Millet, R.D. Braatz, M.Z. Bazant, M. Eikerling, I. Staffell, P. Balcombe, Y. Shao-Horn, H. Schafer, Water electrolysis: from textbook knowledge to the latest scientific strategies and industrial developments, *Chem. Soc. Rev.* 51 (2022) 4583–4762, <https://doi.org/10.1039/d0cs01079k>.

[48] F. Yang, Y. Luo, Q. Yu, Z. Zhang, S. Zhang, Z. Liu, W. Ren, H.M. Cheng, J. Li, B. Liu, A durable and efficient electrocatalyst for saline water splitting with current density exceeding 2000 mA cm<sup>-2</sup>, *Adv. Funct. Mater.* 31 (2021) 2010367, <https://doi.org/10.1002/adfm.202010367>.